Cell Reports

Article

Tspan6 stimulates the chemoattractive potential of breast cancer cells for B cells in an EV- and LXR-dependent manner

Graphical abstract

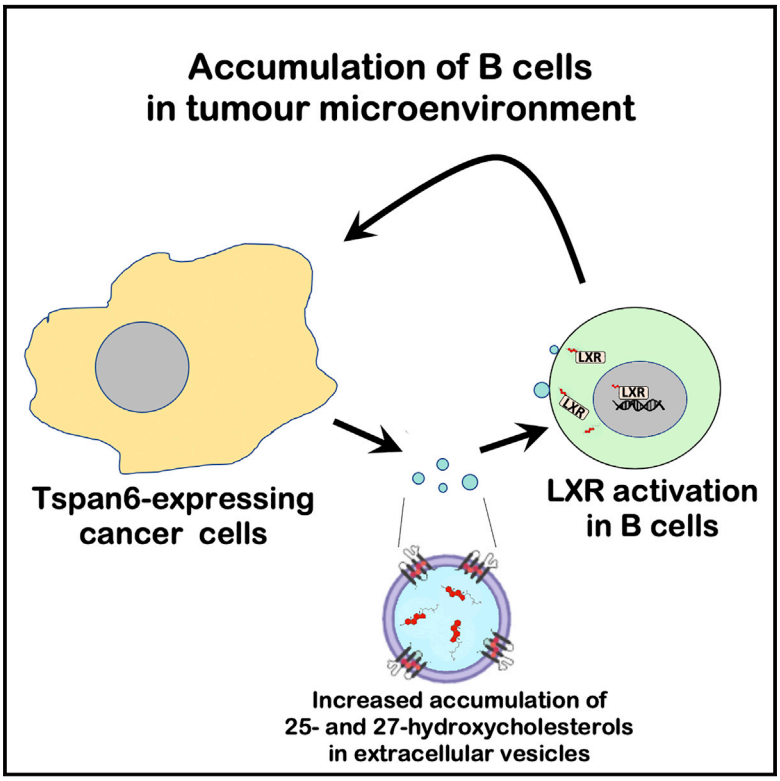

Highlights

- Tspan6 regulates recruitment of B cells to the tumor microenvironment
- Tspan6 controls migration of B cells by cell-derived extracellular vesicles (EVs)
- Tspan6 facilitates accumulation of hydroxycholesterols in EVs
- Migration of B cells involves activation of LXR-dependent pathway

Authors

Guerman Molostvov, Mariam Gachechiladze, Abeer M. Shaaban, ..., Steven van Laere, Heather M. Long, Fedor Berditchevski

Correspondence

h.m.long@bham.ac.uk (H.M.L.), f.berditchevski@bham.ac.uk (F.B.)

In brief

B lymphocytes play an important role in anti-cancer immunity. Molostvov et al. demonstrate that migration and recruitment of B cells to breast cancer tissues are controlled by Tspan6 expression on cancerous cells. The underlying mechanisms involve increased accumulation of hydroxycholesterols on cell-derived extracellular vesicles and activation of the LXR pathway.

Molostvov et al., 2023, Cell Reports *42*, 112207
March 28, 2023
https://doi.org/10.1016/j.celrep.2023.112207

CellPress

Cell Reports

CellPress
OPEN ACCESS

Article

Tspan6 stimulates the chemoattractive potential of breast cancer cells for B cells in an EV- and LXR-dependent manner

Guerman Molostvov,[1] Mariam Gachechiladze,[1,2] Abeer M. Shaaban,[1] Steven Hayward,[1] Isaac Dean,[3] Irundika H.K. Dias,[4] Nahla Badr,[1,5] Irini Danial,[1] Fiyaz Mohammed,[3] Vera Novitskaya,[1] Liliia Paniushkina,[6] Valerie Speirs,[7,8] Andrew Hanby,[7] Irina Nazarenko,[6,9] David R. Withers,[3] Steven van Laere,[10] Heather M. Long,[3,*] and Fedor Berditchevski[1,11,*]

[1]Institute of Cancer and Genomic Sciences, The University of Birmingham, Edgbaston, Birmingham B15 2TT, UK
[2]Department of Clinical and Molecular Pathology, Palacky Univerzity, 7779 00 Olomouc, Czech Republic
[3]Institute of Immunology and Immunotherapy, The University of Birmingham, Edgbaston, Birmingham B15 2TT, UK
[4]Aston Medical Research Institute, Aston Medical School, Aston University, Birmingham B4 7ET, UK
[5]Department of Pathology, Faculty of Medicine, Menoufia University, Shebin El-Kom, Egypt
[6]Faculty of Medicine, Institute for Infection Prevention and Hospital Epidemiology, Medical Center - University of Freiburg, 79106 Freiburg, Germany
[7]Leeds Institute of Medical Research, University of Leeds, St James's University Hospital, Leeds LS9 7TF, UK
[8]Institute of Medical Sciences, University of Aberdeen, Aberdeen AB25 2ZD, UK
[9]German Cancer Consortium (DKTK), Partner Site Freiburg and German Cancer Research Center (DKFZ), 69120 Heidelberg, Germany
[10]Translational Cancer Research Unit Center for Oncological Research, University Antwerp, Antwerp 2610, Belgium
[11]Lead contact
*Correspondence: h.m.long@bham.ac.uk (H.M.L.), f.berditchevski@bham.ac.uk (F.B.)
https://doi.org/10.1016/j.celrep.2023.112207

SUMMARY

The immune microenvironment in breast cancer (BCa) is controlled by a complex network of communication between various cell types. Here, we find that recruitment of B lymphocytes to BCa tissues is controlled via mechanisms associated with cancer cell-derived extracellular vesicles (CCD-EVs). Gene expression profiling identifies the Liver X receptor (LXR)-dependent transcriptional network as a key pathway that controls both CCD-EVs-induced migration of B cells and accumulation of B cells in BCa tissues. The increased accumulation oxysterol ligands for LXR (i.e., 25-hydroxycholesterol and 27-hydroxycholesterol) in CCD-EVs is regulated by the tetraspanin 6 (Tspan6). Tspan6 stimulates the chemoattractive potential of BCa cells for B cells in an EV- and LXR-dependent manner. These results demonstrate that tetraspanins control intercellular trafficking of oxysterols via CCD-EVs. Furthermore, tetraspanin-dependent changes in the oxysterol composition of CCD-EVs and the LXR signaling axis play a key role in specific changes in the tumor immune microenvironment.

INTRODUCTION

Unraveling the molecular mechanisms governing the complex cross-talk between cancer cells and other cell types within the tumor microenvironment (TME) is essential for understanding tumor development and progression as well as developing new therapeutic strategies. Different cell types within the TME play key roles in regulating primary cancer growth, directing metastatic progression, and defining antitumor host immune responses.[1,2]

The immune cell composition within the TME is controlled by an elaborate network of communications involving chemokines, cytokines, and growth factors produced by tumor-infiltrating immune cells, cancer cells, and other cell types, such as vascular endothelium and tumor-associated fibroblasts. While the specific contribution of various types of tumor-infiltrating T cells and macrophages to tumor development and host immune responses in breast cancer (BCa) is becoming increasingly clear,[3] there is a paucity of data on the functions of tumor-infiltrating B lymphocytes (TIL-Bs). It has been proposed that TIL-Bs can enhance cellular antitumor immunity by serving as antigen-presenting cells for T cells, contributing to organizing tertiary lymphoid structures and secreting polarizing cytokines.[4] Importantly, TIL-Bs were found to be oligoclonal indicating that they have undergone somatic hypermutation.[5] Therefore, the abundance of TIL-Bs may contribute to more potent and sustained humoral antitumor immunity. Indeed, higher numbers of TIL-Bs correlated with better survival of patients with certain subtypes of BCa.[6–8] Notably, TIL-Bs were shown to respond to B cell receptor stimulation to produce B cell cytokines and immunoglobulins *in situ*.[7] Furthermore, experiments involving mouse models of BCa TIL-B have demonstrated that B cells are essential for effective responses to immune checkpoint inhibitor-based therapies.[9] In spite of growing realization of the

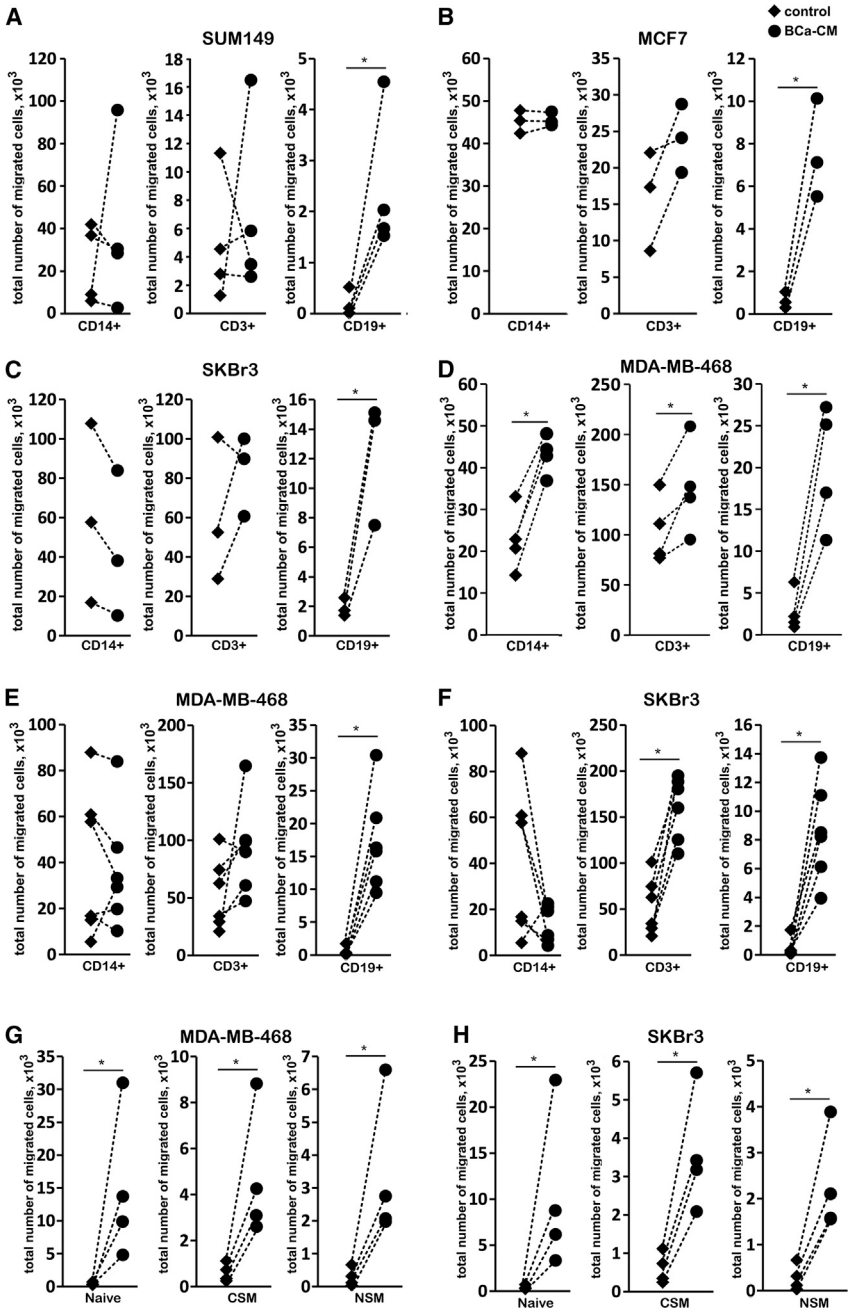

Figure 1. Media conditioned by BCa cells specifically enhances migration of B cells

Media conditioned by human BCa cell lines (BCa-CM) were used as chemoattractants for purified human PBMCs in transwell migration assays (three to four healthy donors in A–D, G, and H or six BCa patients in E and F). PBMCs were allowed to migrate for 16–18 h and subsequently profiled by flow cytometry. "Control"- growth media. Naive, class switched memory (CSM), and non-class switched memory (NSM) B cells were defined as $CD19^+$ $CD27^-IgD^+$, $CD19^+CD27^+IgD^-$, and $CD19^+CD27^+$ IgD^+ cells, respectively. Numbers observed in separate experiments are connected by dotted lines. p values were calculated using two-tailed t test and are indicated on graphs. *$p < 0.05$.

importance of TIL-Bs in BCa, the molecular pathways that control B cell infiltration into cancerous tissues remain poorly studied. Chemokines CCL19, CCL21, and CXCL13 have been proposed to be involved.[10] Identification of the key molecular mechanisms governing recruitment, retention, and functional diversification of B cells in BCa is critical for determining their full impact on tumor and progression and further development of immunotherapies.

In addition to the critical role played by soluble chemokines, cytokines, and growth factors, cancer cells communicate and modify the tumor microenvironment by secreting vesicles.[11] Extracellular vesicles (EVs) secreted by cancer cells (CCD-EVs) function as powerful signaling organelles through activation of receptor-specific pathways and by inducing specific changes in transcriptional and translational programs in the target cells.[12] Here we found the chemoattractive potential of BCa cells for B lymphocytes is regulated by CCD-EVs and involves activation of Liver X receptors (LXRs), nuclear receptors for oxysterols, in B cells. LXRs and their most potent oxysterol ligands (i.e., 25-hydroxycholesterol and 27-hydroxycholesterol) are known to contribute to shaping humoral and adaptive immune responses.[13,14] Thus, the LXR-oxysterol signaling axis has been reported to contribute to the communication between tumor-associated macrophages and T cells in breast and other types of cancer.[15] However, the involvement of oxysterols and LXR proteins in B cell biology in the context of cancer and in the formation of the tumor immune microenvironment remains completely unknown.

Various members of the transmembrane proteins of the tetraspanin superfamily are abundant on EVs, and it has become increasingly apparent that they play an important role in the regulation of biological activities of EVs.[16] One possible mechanism involves tetraspanin-dependent selective recruitment of adhesion receptors and proteolytic enzymes that direct EVs to their specific cellular targets.[16] It was also demonstrated that modulation of tetraspanin expression in vesicle-producing cells leads to specific changes in EV-associated micro RNAs.[17] Here we demonstrated that tetraspanins can regulate the oxysterol composition of EVs. Specifically, we found that tetraspanin 6 (Tspan6) facilitates the accumulation of 25-hydroxycholesterol and 27-hydroxycholesterol in CCD-EVs. Accordingly, CCD-EVs from Tspan6-expressing BCa cells were more potent in stimulating the LXR-dependent migration

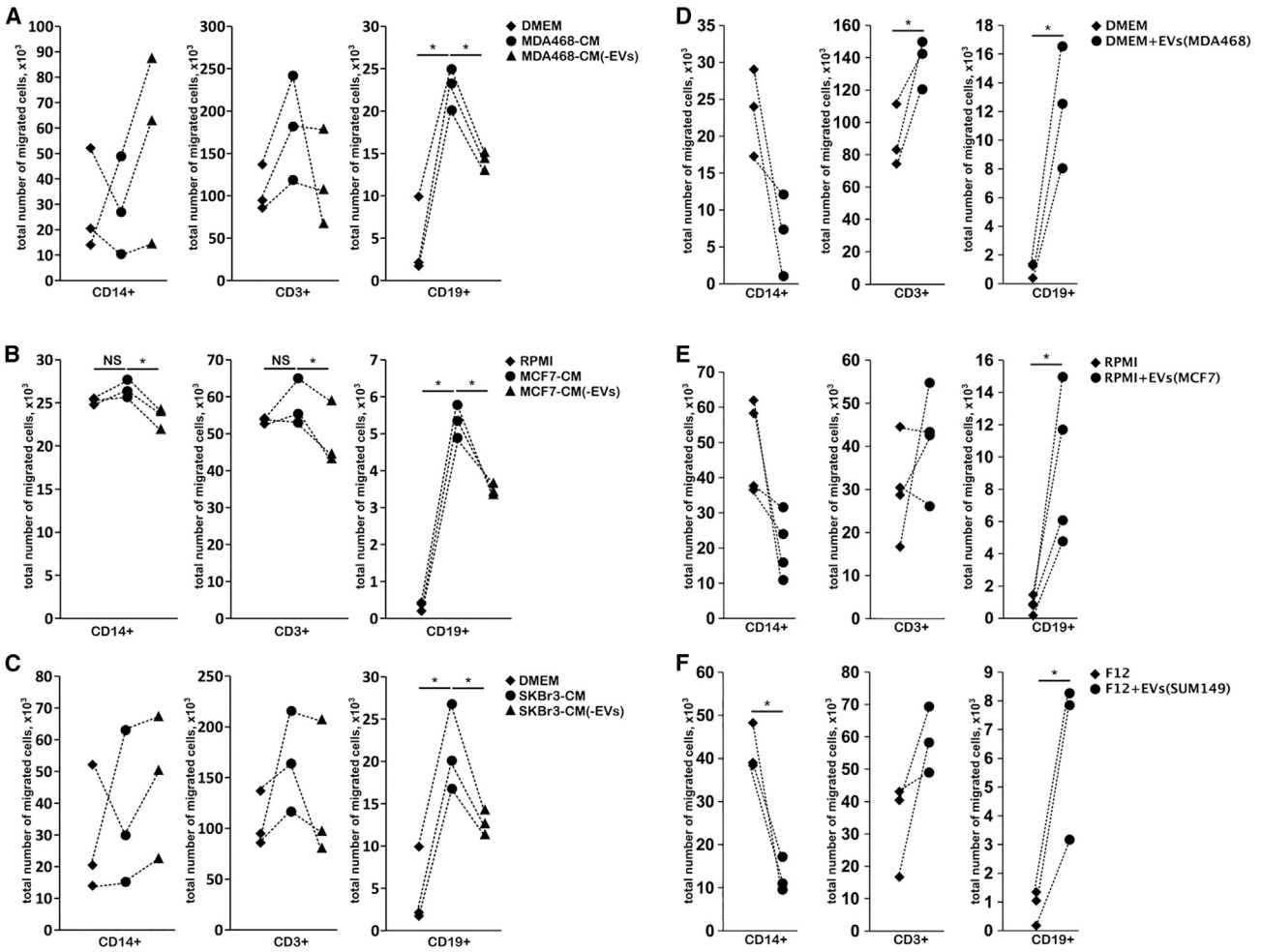

Figure 2. Critical role of EVs in the chemoattractive potential of BCa cells for B cells

(A–C) Media conditioned (CM) by MDA-MB-468 (A), MCF-7 (B), or SKBr3 cells were depleted of EVs ("-EVs") by centrifugation. Purified PBMCs (three healthy donors) were allowed to migrate for 18 h and subsequently profiled by flow cytometry. "CM" – conditioned media not depleted of EVs was included as a positive control.

(D–F) EVs purified from supernatants conditioned by MDA-MB-468, MCF7, and SUM149 cells were added to appropriate growth media without supplements and used as chemoattractants (DMEM + EVs). Purified PBMCs (three healthy donors) were allowed to migrate for 18 h and subsequently profiled by flow cytometry. "Control"- DMEM with no supplements. Numbers observed in separate experiments are connected by dotted lines. p values were calculated using a two-tailed t test and are indicated on graphs. *$p < 0.05$.

of B cells. Furthermore, we showed that the LXR-dependent gene expression signature in B cells was associated with Tspan6-positive BCa cells enriched in TIL-B. These results reveal that tetraspanins control the oxysterol composition of EVs, thus allowing targeted delivery of lipids to the immune cells in the tumor microenvironment.

RESULTS

BCa cells stimulate migration of B lymphocytes

To investigate the contribution of cancer cells to the immune microenvironment in BCa, we evaluated the chemoattractive potential of media conditioned by established BCa model cell lines (BCa-CM) for the main subtypes of immune cells in peripheral blood mononuclear cells (PBMCs) from healthy donors and BCa patients (Table S1). In initial experiments we demonstrated that media conditioned by BCa cell lines derived from different molecular subtypes consistently increased migration of B cells present in the blood of healthy donors (Figures 1A–1D). By contrast, the effect of CM on migration of monocytes and T cells varied between breast cancer lines (Figure 1). BCa-CM equally affected migration of major B cell subtypes (i.e., naive, class switched memory cells [CSMs], and non-switched memory [NSM]) (Figures 1G and 1H). Similarly, BCa-CM stimulated migration of B cells from the blood of BCa patients (Figures 1E and 1F).

B cell migration is regulated by various chemokines that act via G-protein coupled receptors (GPCRs).[18,19] Profiling media conditioned by several BCa cell lines revealed variable levels of secretion of several known B cell chemokines including interleukin (IL)-8/CXCL8 and CCL20 (Figure S1A), which does not

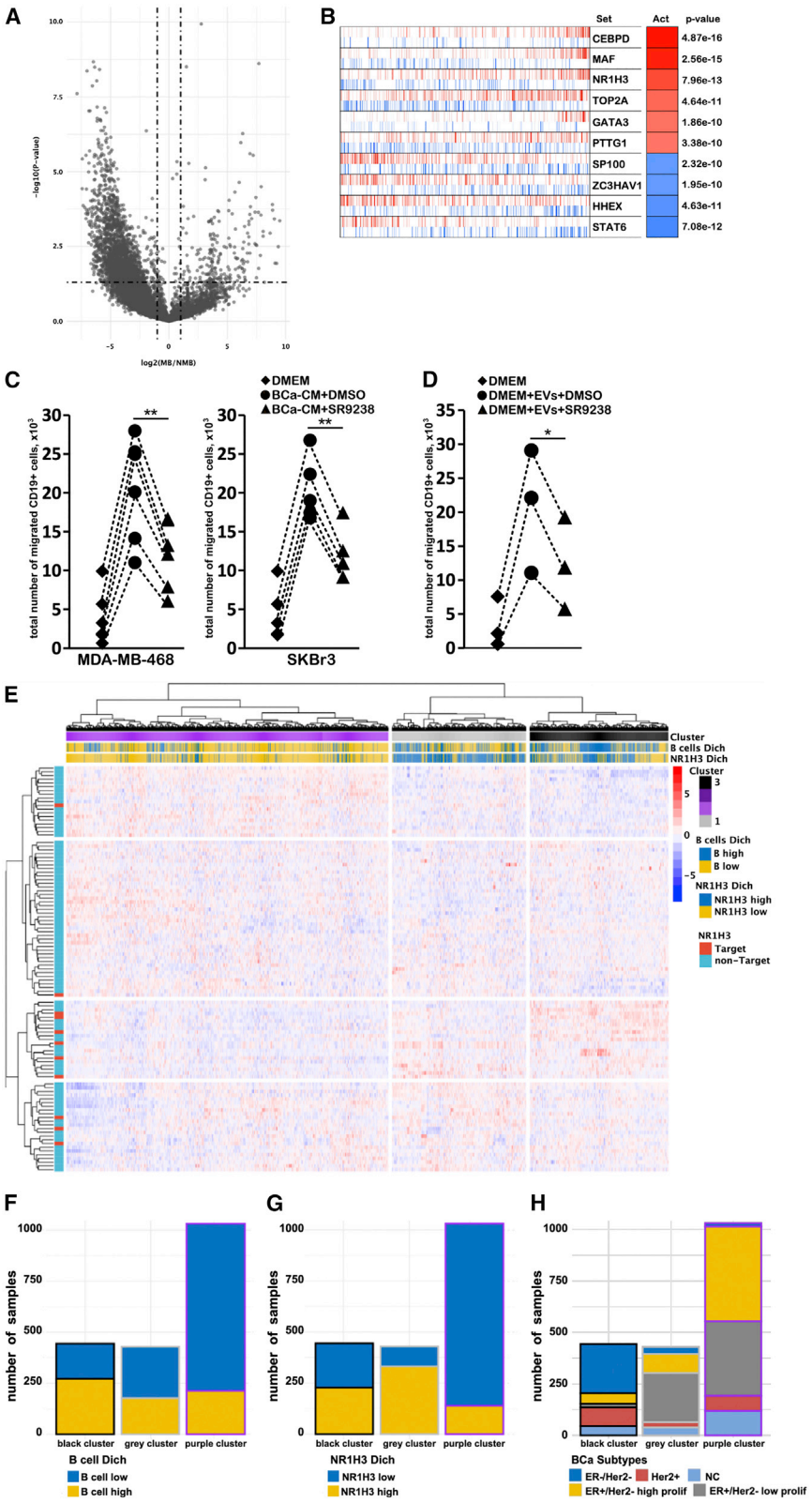

Figure 3. Migration of B cells toward BCa-CM and EVs secreted by BCa cells suppressed involves activation of LXR

(A) Volcano plot is showing differences in gene expression between migratory (MB) and non-migratory B cells (NMB). Each dot in the figure represents a gene. The x axis represents the log2 transformed fold change with positive and negative values denoting genes overexpressed in MB and NMB cells, respectively. The y axis represents the –log10-transformed p value. The horizontal dashed lines indicate the threshold of 5% on the nominal p value, above which differences in gene expression are significant. The vertical dashed lines indicate a threshold of 2 on the fold change.

(B) Representation of the VIPER results for the top 10 most differently activated regulons between MB and NMB cells. Along the x axis, genes are rank-sorted from the one most down-regulated (left) to the one most upregulated (right) in MB vs. NMB cells based on the gene expression analysis. For each regulator, negative and positive targets as identified in the B cell regulon are color-coded blue and red respectively. Based on the distribution of these negative and positive targets, a protein activity score is calculated that is shown in a color-coded format in the column entitled "Act." In addition, also the mRNA expression fold change for each of the reported regulators is shown in a color-coded format in the column entitled "Exp" with grayed-out cells indicating regulons for which mRNA expression levels have not been measured.

(C and D) Purified PBMCs (three to four healthy donors) were pre-treated with S-9238 (1 μM) (or DMSO) and allowed to migrate toward BCa-CM (MDA-MB-468) (C) or media supplemented with EVs purified from BCa-CM (D) using transwell migration assay. Migrated cells were profiled by flow cytometry. Numbers observed in separate experiments are connected by dotted lines. Incubation of cells with DMSO or S-9238 did not affect viability of PBMCs (95%–97%). p values were calculated using a two-tailed t test and are indicated on graphs. *$p < 0.05$; **$p < 0.01$.

(E) Heatmap showing the expression profiles of 1,904 BRCA samples for 127 genes that are upregulated in MB vs. NMB cells, with rows and columns representing genes and samples, respectively. Samples and genes are ordered according to the output of an unsupervised hierarchical cluster analysis (Manhattan linkage, Ward clustering) and resulting dendrograms are shown on top and to the left of the heatmap. Based on differences in gene expression levels of the 127 genes, three sample clusters (indicated with purple, gray, and black colors underneath the top dendrogram) and four gene clusters can be discerned. For each of the 1,904 BRCA samples, dichotomized B cell infiltration (i.e., high vs. low) and NR1H3 activity scores (i.e., high vs. low) are shown using yellow-blue color-coded bars underneath the top dendrogram. For each of the 127 genes overexpressed in NMB cells, a red-blue color-coded bar to the right of the left dendrogram indicates the NR1H3 target gene status. The categorization defined by the color coding for both samples and genes is provided in the legend.

(legend continued on next page)

explain common promigratory properties of different BCa-CMs (shown in Figure 1). Further quantitative ELISA and Luminex analyses demonstrated that the concentration of these and other B cell chemokines (e.g., CXCL12 and CXCL13) in BCa-CM is relatively low (10–800 pg/mL) (Table S2). To investigate whether BCa-induced B cell migration is mediated by these or other chemokines acting via GPCRs, we performed the experiments in the presence of pertussis toxin (PTX), which is known to block the promigratory activity of all known classical B cell chemokines.[20] These experiments demonstrated that while PTX treatment partially suppressed the migration of monocytes, the chemotactic migration of B cells toward BCa-CM was not affected (Figures S1B and S1C). We also confirmed that midkine secreted by BCa cells (Figure S1A) did not contribute to the migration of B lymphocytes toward BCa-CM (Figures S1D and S1E), a mechanism we have previously demonstrated for the accumulation of monocytes in IBC.[21] Collectively, these results suggested that classical B cell chemokines were not essential for the migration of B lymphocytes induced by BCa cells.

EVs secreted by BCa cells stimulate migration of B cells

EVs regulate various aspects of cell migration.[22] Thus, we examined the contribution of BCa-derived EVs (CCD-EVs) in the migration of B lymphocytes toward BCa-CM. Removal of CCD-EVs by centrifugation reduced the chemoattractive potential of BCa-CM for B cells by 35%–45% (Figures 2A–2C). The effect of CCD-EV depletion on the migration of other cell populations was variable (Figures 2A–2C). In reverse experiments, we examined the effect of purified EVs on migration of PBMCs. The addition of purified CCD-EVs secreted by various BCa cell lines increased migration of B cells by 10- to 60-fold (Figures 2D–2F). Notably, when we repeated the experiments using purified EVs produced by GFP-expressing cells (these cells produce GFP-labeled EVs), only migrated B cells were positive for GFP (Figure S2). Together, these results suggested that increased migration of B cells is due to the direct interaction between CCD-EVs and B cells. Although less dramatic, CCD-EVs also increased migration of T cells (by 1.3- to 3.5-fold) (Figures 2D–2F). By contrast, migration of monocytes was decreased when media was supplemented with CCD-EVs. Thus, we concluded that CCD-EVs can change the motility of different types of immune cells with the strongest enhancing effect on B lymphocytes. These results indicated that CCD-EVs are a contributory factor in B cell recruitment and the formation of the immune landscape in BCa.

Migration toward BCa-CM involves the activation of LXR nuclear oxysterol receptors

To examine the nature of the EV-mediated signal(s) that stimulated migration of B cells, we compared expression profiles of B cells migrated toward EVs (MB) and non-migrated B cells (NMB) from the same experiments. The *viper* package was used in combination with a regulon for B cells (*bcellviper* package) to evaluate differences in virtual protein activity levels based on differential expression statistics. In total, 226 proteins revealed differences in protein activity levels between MB and NMB cells at a false discovery rate level inferior to 10% (Figure 3A). Among the top three transcriptional networks identified in this analysis (Figure 3B) we decided to focus on the NR1H3-dependent pathway. NR1H3 encodes LXRα, the nuclear receptor for several oxysterols, which can activate expression programs that are important for chemotaxis.[23,24] Furthermore, only LXR-dependent pathways have (1) the established function in the biology of B cells,[25,26] and (2) a possible link with EVs.[27,28]

To examine whether LXR-dependent signaling pathways contribute to B cell motility induced by the BCa-CM, we repeated migration experiments with conditioned media or CCD-EVs in the presence of SR9238, a reversed agonist for LXR proteins. Strikingly, pre-incubation with SR9238 partially inhibited migration of B cells toward both BCa-CM and BCa-derived EVs (Figures 3C and 3D). Thus, these results indicated that EV-associated oxysterols can stimulate migration of B cells toward BCa-CM.

To examine a possible link between the LXR signaling axis and the accumulation of B cells in human BCa tissues, we examined genes differentially expressed between MB and NMB cells in a series of 1,904 expression profiles of BCa patients (METABRIC series). In total, 1,127 genes were in common between both series. In further analysis, the full set of 127 genes overexpressed in MB cells was evaluated using unsupervised hierarchical cluster analysis. As illustrated in Figure 3E three sample clusters (color-coded black, gray, and purple) and four gene clusters (horizontal) were clearly identifiable. The sample clusters revealed clear differences with respect to B cell infiltration scores ($p < 0.001$; highest in black and gray clusters) (Figures 3E and 3F). Interestingly, the gene cluster enriched for NR1H3 target genes (Figure 3E, $p = 0.011$) was most strongly differentially expressed with the highest mRNA levels in the sample clusters characterized with enhanced B cell infiltration (Figure 3E (black cluster) and Figure 3G). When compared with the molecular subtypes, significant distributional differences were observed ($p < 0.0001$) with the black cluster being enriched for ER−/HER2− and ER−/HER2+ breast tumors (i.e., 74%) and the remaining clusters being dominated by ER+ breast tumors (i.e., 77% in the gray cluster and 80% in the purple cluster). Interestingly, ER+ breast tumors in the gray cluster are predominantly low proliferative (Figure 3H). These results support the notion that the LXR signaling plays an important role in the accumulation of B cells in BCa tissues.

(F) The number of samples (y axis) with low or high dichotomized B cell infiltration scores (respectively blue or yellow) per cluster of breast cancer samples (i.e., black, gray, purple; x axis) are shown in barplot format.
(G) The number of samples (y axis) with low or high dichotomized NR1H3 activation scores (respectively blue or yellow) per cluster of breast cancer samples (i.e., black, gray, purple; x axis) are shown in barplot format.
(H) The number of samples (y axis) according to the breast cancer subtypes per cluster of breast cancer samples (i.e., black, gray, purple; x axis) are shown in barplot format. Breast cancer subtypes are color-coded as shown in the legend underneath the plot with NC indicating breast cancer samples that are not classified.

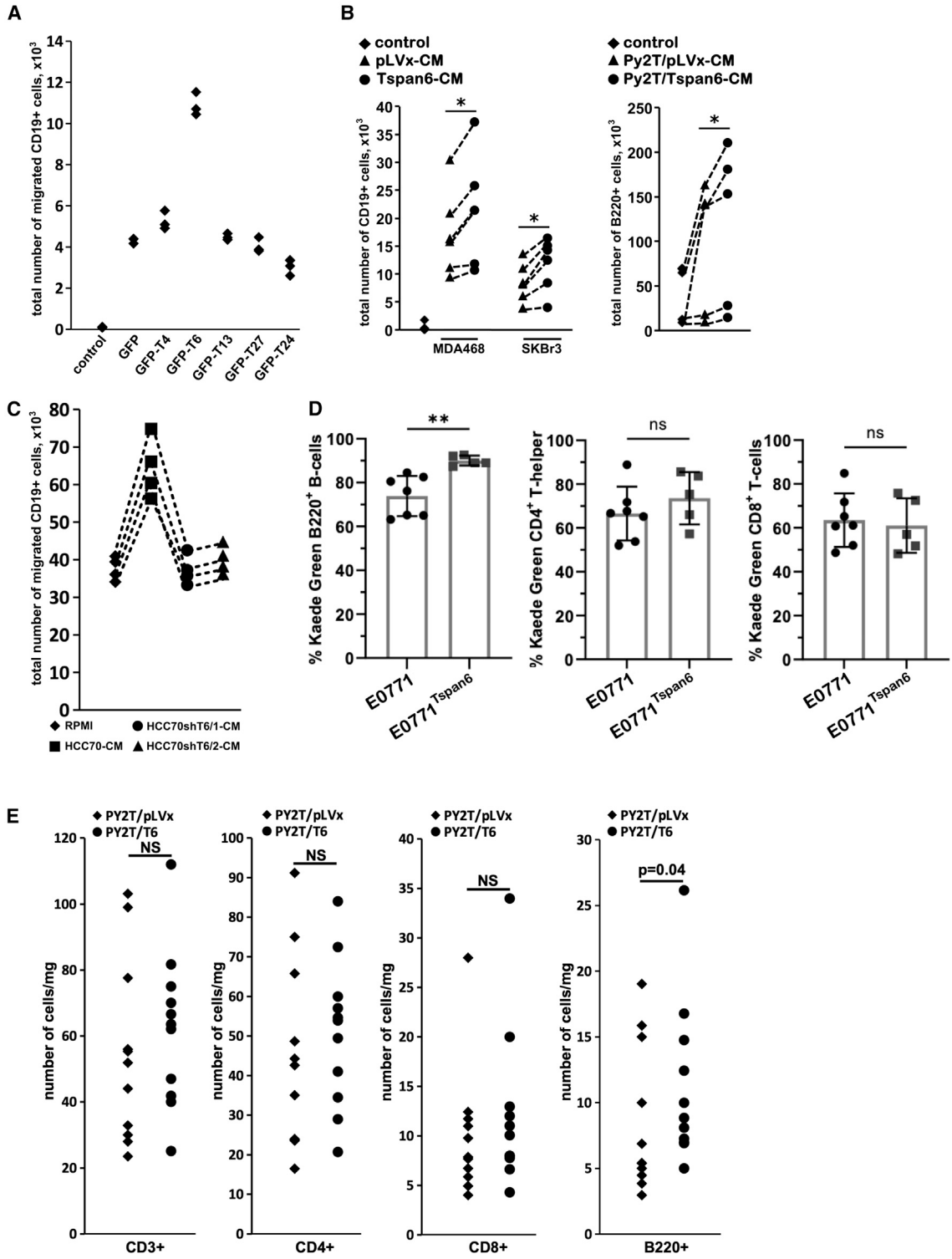

Figure 4. Tspan6 regulates the chemoattractive potential of tumor cells for B lymphocytes

(A) Media conditioned by SUM149 cells expressing various GFP-tagged tetraspanins were used as chemoattractant for purified human PBMCs. PBMCs were allowed to migrate for 16–18 h and migrated B cells were identified by flow cytometry using anti-CD19 mAb.

(B) Media conditioned MDA-MB-468 (MDA468), SKBr3, and PY2T cells were used as chemoattractants for human PBMCs purified from healthy donors (left and middle panels) or mouse splenocytes (right panel). Purified PBMCs/splenocytes were allowed and subsequently profiled by flow cytometry. "Control" - growth

(legend continued on next page)

Tspan6 regulates migration of B cells

Tetraspanin proteins are abundant on various types of EVs and known to regulate their functionalities. We hypothesized that tetraspanins expressed by BCa cells may be involved in LXR-dependent migration of B cells by changing the oxysterol composition of CCD-EVs. Earlier studies demonstrated that various tetraspanins can physically bind cholesterol, and the crystal structure of the tetraspanin CD81 revealed a bound cholesterol molecule within a hydrophobic intramembrane central cavity created by all four TM helical domains.[29,30] Two polar CD81 TM residues, Asn^{18} (TM1) and Glu^{219} (TM4), contributed to stabilizing the cholesterol backbone by mediating hydrogen bonding interactions with the hydroxyl moiety. Although Glu^{219} is not preserved across all tetraspanin family members, tetraspanins encompass additional polar side chains within their TM domains, raising the possibility that they have evolved to not only bind cholesterol but also oxygenate derivatives of cholesterol (i.e., oxysterol LXR ligands). Indeed, if the docking mode of these oxysterols is similar to that seen in the CD81-cholesterol model, we would envisage that specific inward cavity facing polar residues within tetraspanin TM regions, which are located closer to putative TM-extracellular interfaces, may be able to coordinate the additional hydroxyl groups present in oxysterols. We began addressing this possibility by investigating whether tetraspanins could contribute to the chemoattractive potential of BCa cells via CCD-EV-induced activation of LXR in B cells. Specifically, we focused on tetraspanins that conform to the aforementioned structural requirements and whose expression is known to be affected in BCa (i.e., Tspan4, Tspan6, Tspan13, CD151/Tspan24, and CD82/Tspan27 [Figure S3]). The initial experiments were performed using SUM149 cells that express low or undetectable endogenous levels of these tetraspanins (Table S3). The ectopically introduced tetraspanins were GFP-tagged to monitor their expression levels (Figure S4). Of these tetraspanins only Tspan6 could consistently increase the chemoattractive potential of SUM149 cells for B cells (Figure 4A). Similarly, Tspan6 enhanced the chemoattractive potential of other human BCa cell lines and mouse mammary carcinoma cells (Figure 4B). Conversely, knockdown of Tspan6 in Tspan6-positive BCa cells decreased their chemoattractive potential for B cells (Figure 4C). To substantiate these findings further, we used two syngeneic mouse models to examine the role of Tspan6 in the recruitment of B cells to mammary carcinomas *in vivo*. The Kaede transgenic mice express a photoconvertible fluorescent protein (Kaede green-to-red) and can be used to monitor the recruitment of immune cells to different tissues including transplanted syngeneic tumors.[31,32] Tspan6-negative E0771 mouse mammary carcinoma cells and E0771 cells expressing mouse Tspan6 were implanted into the mammary fat pad and recruitment of lymphocytes to the tumors was analyzed 48 h after photoconversion, which labeled the entire CD45+ compartment of the tumor to Kaede Red+. The proportion of newly entering Kaede Green+ B cells was significantly increased in Tspan6-expressing E0771 tumors, indicating that these tumors attracted more B cells when compared with Tspan6-negative tumors (Figures 4D and S5). In comparison, the proportion of Kaede Green+ T cells within the two tumors was not significantly different, indicating a B cell-specific effect (Figures 4D and S5). Additional experiments involving Py2T mouse mammary carcinoma cells confirmed that Tspan6-expressing tumors are characterized by an increased accumulation of B cells (Figure 4E). Furthermore, the expression of Tspan6 partially suppressed growth of Py2T tumors (Figure S6). Collectively, these experiments provide direct evidence that Tspan6 expression enhances B cell migration *in vitro* and *in vivo* and this correlated with decreased growth of the tumors.

Tspan6 relies on EV-associated oxysterols to regulate the chemoattractive potential of BCa cells for B cells

The Tspan6-dependent increase in the chemoattractive potential of BCa cells for B cells was negated when conditioned media was depleted of CCD-EVs (Figure 5A). Conversely, CCD-EVs produced by Tspan6-expressing cells were more potent in stimulating B cell migration when compared with EVs produced by Tspan6-negative cells (Figure 5B). As our data show that migration of B cells toward CCD-EVs is controlled by the LXR-dependent pathway (Figures 3C and 3D), we investigated whether the increase in the chemoattractive potential of CCD-EVs produced by Tspan6 expressing BCa cells is also linked to the activation of LXR. Experiments involving the inverse LXR agonist demonstrated that suppression of LXR activation negated the difference between EVs secreted by Tspan6-negative and Tspan6-positive BCa cells (Figure 5C). As the quantity of EVs produced by BCa cells was not affected by the expression of Tspan6 (Figure 5D), we concluded that the Tspan6-dependent increase in the chemoattractive potential of cell-derived EVs is likely to be related to differences in oxysterol composition of the vesicles.

We hypothesized that Tspan6 may be involved in transport of cellular oxysterols to EVs (see above). To address this, we first generated an I-TASSER derived model of Tspan6 encompassing residues M1-V245 (Figure 6A, left panel). The model displays a similar secondary topology to that of the CD81 crystal structure, forming a cone-like architecture with a distinct large intramembrane cavity within the transmembrane region (Figure 6A, middle and right panels). Then we used high

media. Shown are the results of the experiments using PBMCs from blood of six human donors and splenocyte from five animals. Numbers observed in separate experiments are connected by dotted lines. p values were calculated using a two-tailed t test and are indicated on graphs. *$p < 0.05$.

(C) Media conditioned by HCC70 cells (HCC70-CM) of HCC70 cells stably depleted of Tspan6 (HCC70shT6/1-CM and HCC70shT6/2-CM) were used as chemoattractant for purified human B cells. PBMCs were allowed to migrate for 16–18 h and migrated B cells were identified by flow cytometry using anti-CD19 mAb.

(D) E0771/pLVx and E0771/Tspan6 cells were injected into mammary fat pads of Kaede mice and tumors were allowed to grow until they reached approximately 60–80 $mm.^3$ Photoconversion of the "Kaede Green" protein to the converted "Kaede Red" version was achieved by exposing tumors to UV light. Proportion of Kaede $Green^+$ $B220^+$ B cells, $CD4^+$ T cells, and $CD8^+$ T cells infiltrating E0771 (n = 7) and $E0771^{TSPAN6}$ (n = 5) tumors 48 h after tumor photoconversion. Representative of two independent experiments. All migration experiments were performed using transwell migration settings. p values were calculated using a two-tailed t test and one-way ANOVA, and are indicated on graphs. **$p < 0.01$.

(E) PY2T/pLVx and PY2T/Tspan6 cells were injected contralaterally into mammary fat pads of 10 FBV mice. Tumor-infiltrating lymphocytes were identified by flow cytometry using specific mAbs. p values were calculated using a two-tailed t test and are indicated on graphs.

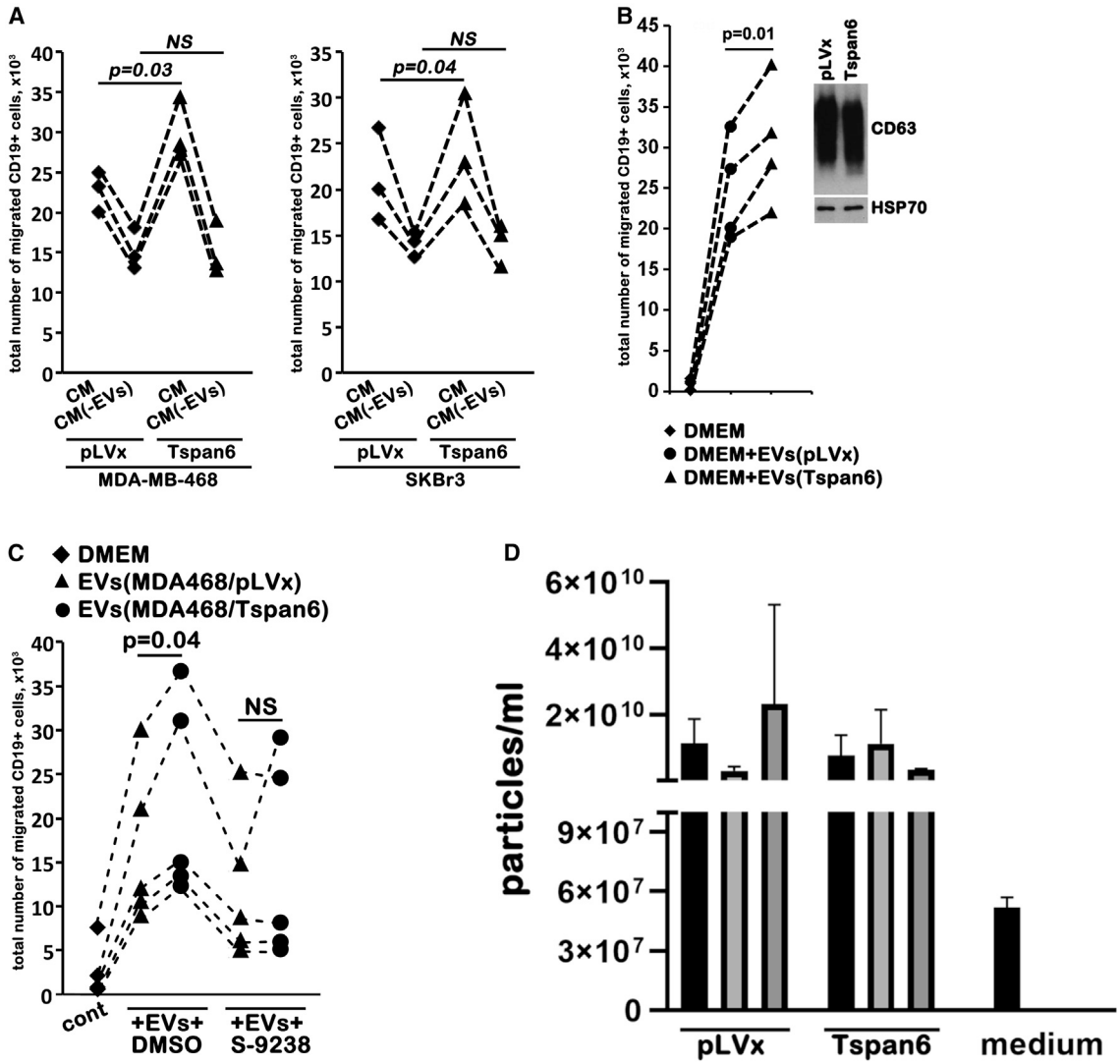

Figure 5. EVs play a critical role in Tspan6-dependent regulation of the chemoattractive potential of tumor cells for B lymphocytes

(A) Media conditioned (CM) by the control (pLVx) or Tspan6-expressing MDA-MB-468 (or SKBr3) cells was depleted of EVs ("-EVs") by centrifugation. Purified PBMCs (three healthy donors) were allowed to migrate for 18 h and subsequently profiled by flow cytometry. CM not depleted of EVs was included as a positive control. p values were calculated using a two-tailed t test and are indicated on graphs.

(B) EVs purified from MDA468/pLVx-CM and MDA468/Tspan6-CM were added to DMEM without supplements and used as chemoattractants. Purified PBMCs (four healthy donors) were allowed to migrate for 18 h and subsequently profiled by flow cytometry. "Control" - DMEM with no supplements. Amounts of EVs added to DMEM were adjusted according to western blot with anti-CD63 mAb (shown results of a representative blot). p values were calculated using a two-tailed t test and are indicated on graphs.

(C) Purified PBMCs (three donors) were pre-treated with S-9238 (1μM) (or DMSO) and allowed to migrate toward media supplemented with EVs purified from MDA-MB-468/pLVx and MDA-MB-468/Tspan6 CM. Numbers observed in separate experiments are connected by dotted lines. p values were calculated using two-tailed t test and are indicated on graphs. Note, EV depletion negated differences in the chemoattractive potentials of EVs produced by Tspan6-positive and Tspan6-negative cells. Migration experiments in (A)–(C) were performed using transwell migration settings.

(D) Expression of Tspan6 does not affect the production of EVs by BCa cells. An equal number of the MDA-MB-468/pLVx and MDA-MB-468/Tspan6 cells was seeded and cultured for 48 h in the serum-free medium containing 1% BSA. NTA analysis on the CM was performed in biological triplicates ("1," "2," and "3" on the diagram) and technical duplicates. The background particle count in medium was measured to estimate the portion of particles of non-cellular origin, floating in the commercial medium used for cell culture.

ambiguity driven protein-protein DOCKing (HADDOCK) program to model a possible interaction interface between Tspan6 and two principal oxysterol LXR ligands: 25-hydroxycholesterol (25-HC) and 27-hydroxycholesterol (27-HC, also known as 26-hydroxycholesterol[33]). Importantly, both 25-HC and 27-HC, which are known to function as chemoattractants, were previously found in BCa-derived EVs.[34] Most Tspan6 residues that were used to restrain docking to the 25-HC and 27-HC moiety corresponded to CD81 amino acids previously implicated in cholesterol binding (Thr[25],

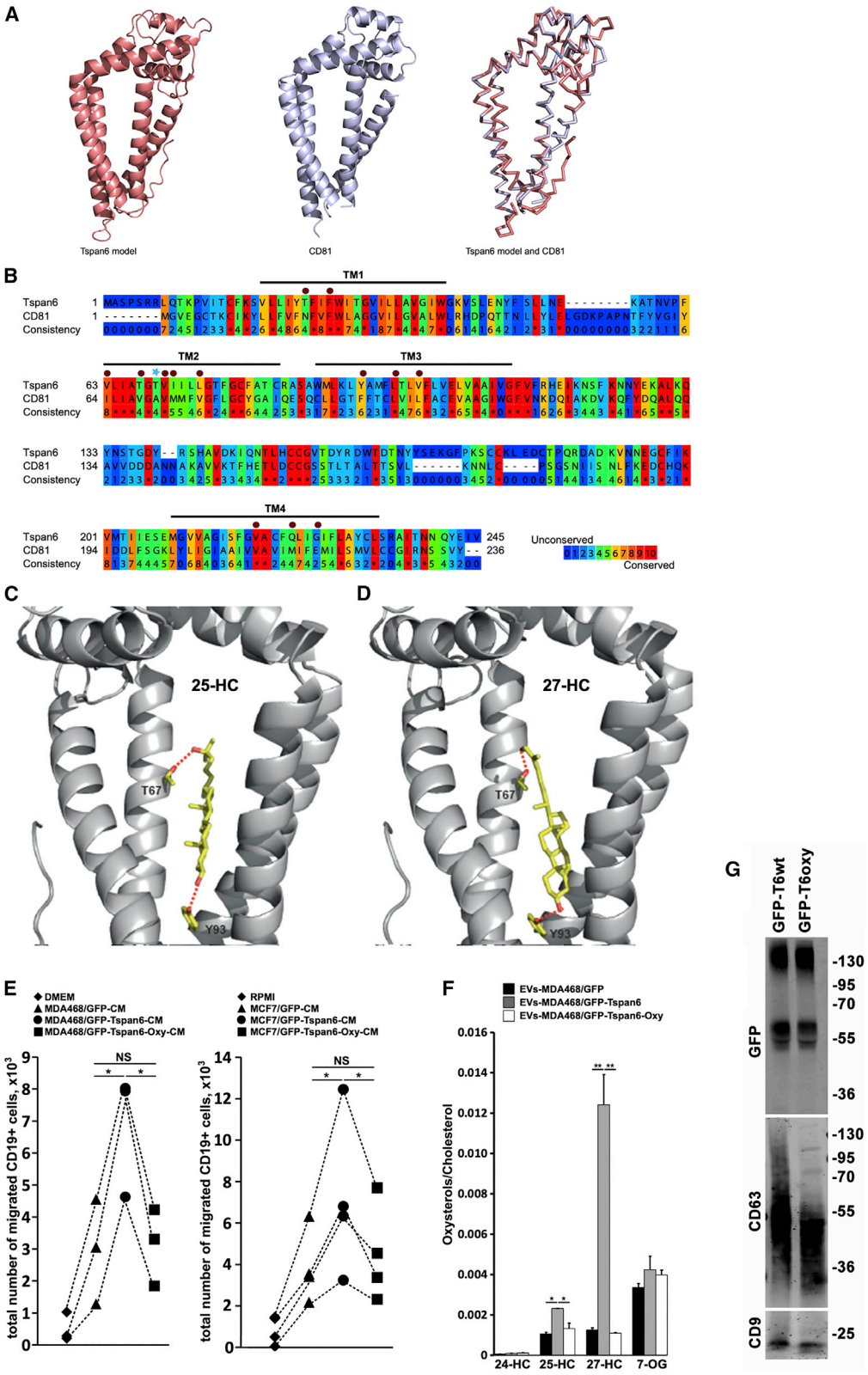

(legend on next page)

Phe[28], Val[63], Val[70], Ile[71], Leu[74], Tyr[93], Leu[97], Val[100], Phe[219], Ile[222], and Gln[223]) (Figure 6B). In the resulting models 25- and 27-HC consistently slotted into the large intramembrane cavity with minimal structural rearrangement. More specifically, the putative 25-/27-HC-Tspan6 interface was predominantly stabilized by a series of non-polar interactions mediated by aromatic and non-aromatic residues. In addition, the Tspan6 residue Thr[67] emanating from TM2 was predicted to form a hydrogen bonding interaction with the additional hydroxyl group (positions 25 and 27) in the cholesterol backbone (Figures 6C and 6D). To validate this putative docking mode, we substituted Thr[67] to Ala (Tspan6-Oxy(−)) and compared its chemoattractive potential with Tspan6wt. Sequence alignments of the TM2 region of the Tspan family highlighted that Alanine could be tolerated at this position while preserving Tspan6 structural integrity. While expressed at the level similar to that of the wild-type protein, media conditioned by the Tspan6-Oxy(−) mutant did not stimulate B cell migration beyond the level seen for Tspan6-negative cells (Figure 6E). Analysis of the main oxysterol ligands for LXR by quantitative mass spectrometry demonstrated that the level of 25-HC and 27-HC in CCD-EVs secreted by Tspan6-expressing cells was ~3- to 7-fold higher than that seen in CCD-EVs produced by the control, Tspan6-negative cells (Figure 6F). Furthermore, we found that crude cellular membranes of Tspan6-expressing cells also had higher levels of 25-HC and 27-HC than those extracted from Tspan6-negative cells (Figure S7A). By contrast, total cellular levels of these oxysterols (which also included cytoplasmic pools of 25-HC and 27-HC) were comparable (Figure S7B). These results indicated that Tspan6 is specifically involved in transport of these oxysterols into EVs rather than regulating their biosynthesis and intracellular metabolism. Importantly, although Tspan6wt and Tspan6-Oxy(-) mutant are recruited to EVs in comparable quantities (Figure 6G), 25-HC and 27-HC levels in CCD-EVs produced by cells expressing Tspan6-Oxy(−) mutant were similar to that of the control, Tspan6-negative cells, and well below that detected in CCD-EVs produced by Tspan6wt-expressing cells (Figure 6F). These results further strengthen the EVs-specific link between Tspan6 and transport of oxysterols.

Expression of Tspan6 is correlated with the recruitment of B cells to BCa tissues

Two approaches were used to further investigate the clinical relevance of the expression of Tspan6, oxysterols and accumulation of B cells in BCa. First, we evaluated the prognostic relevance of *TSPAN6* mRNA and virtually inferred protein activity levels in the METABRIC series of 1,904 BCa samples. These analyses revealed that overexpression or hyperactivation of Tspan6 is associated with improved survival (LogRank-test; $p < 0.001$ and $p < 0.001$, respectively) (Figures 7A and 7B). In addition, a multivariate Cox regression analysis demonstrated that the low Tspan6 protein activity levels predicted overall survival (OS) independently of the major BCa molecular subtypes (Figure 7C). Accordingly, expression of Tspan6 protein in BCa tissue correlated with the improved disease-free survival (Figure 7D), thereby validating our *in silico* results on the METABRIC series. Further, we correlated the dichotomized Tspan6 protein activity scores with the sample clustering pattern described in Figure 3E. The sample clusters revealed clear differences with respect to the distribution of the dichotomized Tspan6 protein activity scores ($p < 0.001$; highest in black and gray clusters) (Figure 7E). In addition, we compared the average expression levels of the NR1H3 target genes among the black, gray, and purple clusters (Figure 7F). These analyses revealed that the NR1H3 target gene expression was most pronounced in the cluster with elevated B cell infiltration scores. and Tspan6 protein activity levels, suggesting that all three parameters are linked. Importantly, analysis of B cell accumulation in BCa tissues further confirmed a significant positive relationship between Tspan6 expression and accumulation of CD20+ lymphocytes in BCa tissues (Figure 7G). Taken together these results indicated that the expression of Tspan6 is linked to the NR1H3-dependent accumulation of B cells in BCa tissues *in vivo*.

DISCUSSION

In this study, we have established that tetraspanin-dependent changes in the lipid composition of EVs secreted by cancer cells can shape the tumor immune microenvironment in BCa. Specifically, we demonstrated that Tspan6 acting via BCa cell-derived

Figure 6. Mutation of the putative 27-HC binding site in Tspan6 abolishes the increase in the chemoattractive potential of Tspan6-expressing BCa cells

(A) Modeling of Tspan6 structure. Cartoon representation of the Tspan6 model generated by I-TASSER (C-score = −0.11) (left panel). Cartoon representation of the crystal structure of CD81 (PDB code 5TCX) (middle panel). Superimposition of Tspan6 and CD81 in ribbon format.

(B) Sequence alignment of Tspan6 and CD81. Sequences were obtained from Uniprot (accession numbers O43657 [Tspan6] and P60033 [CD81]). Alignment was performed using the PRALINE multiple sequence alignment toolkit[35] with the color scheme showing the degree of amino acid conservation. Regions corresponding to the four transmembrane regions are highlighted. CD81 residues that are within 4A of the cholesterol binding site are shown as red circles.

(C and D) Docking of 25-HC and 27-HC on the I-TASSER derived model structure of Tspan6 using HADDOCK.

(E) Media conditioned by cells expressing wild-type Tspan6 and Tspan6-Oxy mutant (MDA-MB-468 [left panel] or MCF-7 [right panel]) were used as chemoattractant for purified human PBMCs using transwell migration assays (three to four healthy donors). PBMCs were allowed to migrate for 16–18 h and migrated B cells were identified by flow cytometry using anti-CD19 mAb. Numbers observed in separate experiments are connected by dotted lines. p values were calculated using a two-tailed t test and are indicated on graphs. *$p < 0.05$.

(F) Oxysterols in the samples of purified EVs were extracted and analyzed using LC-MS/MS (24-hydroxycholesterol; 24-HC, 25-hydroxycholesterol; 25-HC and 27-hydroxycholesterol; 27-HC).

(G) Recruitment of Tspan6wt and Tspan6-Oxy mutant to the CCD-EVs. EVs secreted by MDA-MB-468/GFP-Tspan6 and MDA-MB-468/GFP-Tspan6-Oxy cells were profiled by western blot using indicated antibodies. Note, similar levels of Tspan6wt and Tspan6-Oxy(-) mutant in samples of CCD-EVs. Shown are the results of a representative blot from two independent experiments.

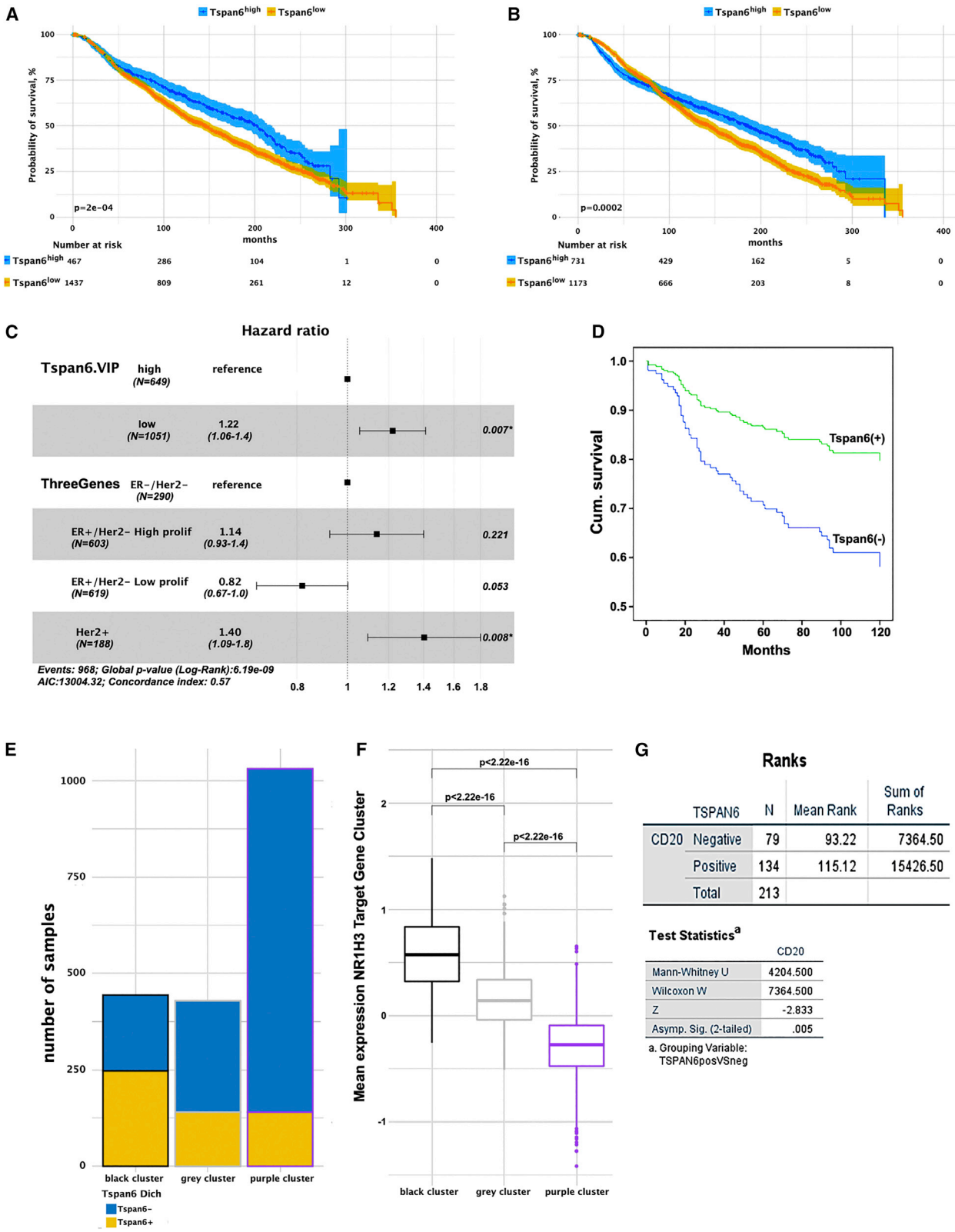

(legend on next page)

EVs (CCD-EVs) facilitates recruitment of B cells to the cancerous tissue. At the molecular level, Tspan6 regulates oxysterol-composition of CCD-EVs, which function as chemoattractants by activating LXR-dependent pathways in B cells. These data demonstrate that cancer cell-associated proteins change the immune landscape of the tumors by modifying lipid composition of CCD-EVs.

It has long been suspected that CCD-EVs contribute to the modulation of the tumor immune microenvironment.[36] Here we demonstrated that CCD-EVs function as carriers to deliver oxysterols to their target cells leading to a specific accumulation of B cells in BCa tissues. The increased density of B cells is known to correlate with a better prognosis in BCa[6] and may explain the improved survival of Tspan6-positive BCa patients in our cohort. In contrast, we found no significant correlation between CD20+ immune cells and patient age, tumor grade, tumor type, and HER2 status in the whole cohort of patients used in our study. Similarly, in the total patient cohort, higher infiltration of CD20+ B cells did not correlate with OS ($p = 0.9$). Only a near-significant correlation was found between CD20 positivity and ER-negative tumors ($p = 0.06$). This may not be entirely surprising, as several previous studies have reported both positive and negative correlations between the magnitude of B cell infiltration and survival of BCa patients (reviewed in Shen et al.[37]). These contrasting observations are likely explained by phenotypic (and functional) heterogeneity of tumor-infiltrating CD20+ B cells as well as genetic variability in the BCa patient cohorts used. A more comprehensive single cell-based RNA sequencing and phenotypic analyses of BCa tissues will be necessary to establish possible links between subtypes of tumor-infiltrating B lymphocytes (e.g., transitional zone B cells, regulatory B cells, plasmablasts), expression of Tspan6, and various clinical parameters.

Our results demonstrate that the LXR-activated transcriptional network has a direct impact on B cell migration. While the underlying molecular mechanisms will require further investigation, it has been reported that activation of LXR in B cells leads to the increased expression of CD38, a transmembrane adenosine 5′-diphosphate-ribosyl transferase with a well-documented promigratory activity in various types of immune cells.[38] LXR activation in B cells was also linked to various key signaling pathways including TGFβ1-and STAT1-dependent signaling networks, which can contribute to cell migration.[39] Finally, a genome-wide analysis of the LXR-dependent transcriptional network in other leukocytes reveals a number of direct LXR-target genes that can directly impact B cell migration.[40]

Various oxysterol species can be detected in exosomes secreted by BCa cells.[34] However, the molecular mechanisms controlling the accumulation of oxysterols in EVs remain completely unknown. Our data demonstrate that Tspan6 is directly involved in this process. While some of the established oxysterol transporters (e.g., members of the ATP-binding cassette transporters, NPC, and other oxysterol-binding proteins) have been detected on EV-produced cancer cells,[41] their role in the transport of various oxysterol species to EVs remains unknown. Furthermore, most of them were absent in vesicles secreted by MDA-MB-468 and MCF-7 cells,[42] two cellular models used in our study. Thus, Tspan6 represents the example of a protein that directly regulates the targeting of oxysterol species to EVs. Importantly, the effect of Tspan6 on oxysterol accumulation in EVs is specific and only affects 25-HC and 27-HC. This excludes the possibility of a more general effect of Tspan6 on the oxysterol metabolism in cells or on the formation/secretion of EVs. Our molecular docking analyses suggest that Tspan6 may bind these oxysterols directly, and, therefore, potentially

Figure 7. Expression of Tspan6 in BCa correlates with better survival and increased accumulation of B cells

(A) KM-plot evaluating differences in overall survival of BCa patients expressing high (blue) and low (yellow) levels of TSPAN6 mRNA (METABRIC samples). The probability of survival is shown on the y axis. Shown are reported p values (log Rank test) and the number of patients at risk per category at discrete time points.

(B) KM-plot evaluating differences in overall survival of BCa patients displaying high (blue) and low (yellow) levels of virtually inferred activity of Tspan6 protein. Shown are reported p values (log Rank test) and the number of patients at risk per category at discrete time points.

(C) Forest plot showing the result of a multivariate Cox proportional hazards analysis comparing the overall survival of BCa patients to both the distribution of the molecular subtypes (i.e., ThreeGenes) and the dichotomized TSPAN6 protein activity score (i.e., Tspan6.VIP). The hazard ratio is plotted along the x axis with a cutoff value of 1, which indicates absence of association between the tested parameter and OS, shown by a vertical dashed line. For each category, except the references (i.e., high TSPAN6 protein activity and ER−/HER2−), point estimates and confidence intervals of the hazard ratios are shown, with positive and negative hazard ratios indicating respectively an increased and decreased risk of an OS event relative to the reference categories. Hazard ratios associated with confidence intervals do not cross the reference line of 1 are significantly different from 1, indicating am effect on OS. Hence, the current forest plot reveals that patients with TSPAN6 low tumors and HER2+ breast cancer are respectively at increased and decreased risk of an OS event relative to their reference categories. Since these results have been obtained using an additive multivariate Cox proportional hazards model, the conclusion stands that both observations are independent from each other. Underneath the forest plot, the global p value, the AIC, and the concordance index of the model are provided.

(D) KM-plot evaluating differences in disease-free survival between BCa patients with high (blue) and low (yellow) expression of Tspan6 evaluated by IHC. Probability of survival is shown in the y axis.

(E) Barplot showing the distribution of the BCa samples classified according the dichotomized Tspan6 activity score in the three METABRIC sample clusters identified using unsupervised hierarchical clustering of the 127 genes overexpressed in MB vs. NMB cells. The sample clusters are indicated along the x axis using the same color names as those reported in the heatmap (Figure 3E). For clarity, the circumference of the bars is colored accordingly. Each bar is further subdivided into two parts that are proportional to the number of samples with active Tspan6 (yellow) or inactive Tspan6 (blue) according the dichotomized Tspan6 activity score. The number of samples per cluster and TSPAN6 activity category is provided along the y axis.

(F) Boxplots comparing the average expression levels of the genes in the gene cluster enriched for NR1H3 targets (Figure 3E) among the three METABRIC sample clusters identified using unsupervised hierarchical clustering of the 127 genes overexpressed in MB vs. NMB cells. The sample clusters are indicated along the x axis using the same color names as those reported in the heatmap (Figure 3E). For clarity, the circumference of the boxplots is colored accordingly. p values resulting from pairwise comparisons of the distribution of averaged expression values between the different clusters using Mann-Whitney *U* test are provided on top of the boxplots.

(G) Immunohistochemical staining of BCa tissue shows a significant correlation (Mann-Whitney test) between Tspan6 expression in the tumor cells and high $CD20^+$ B cell infiltration in the adjacent tumor microenvironment.

function as a transporter of these oxysterol species. Although our results clearly indicate the importance of Thr67 in the second transmembrane domain of Tspan6 for coordinating/trafficking oxysterols to EVs, the presence of polar residues in the corresponding region of other tetraspanins (e.g., Tspan4) does not guarantee the ability to bind/coordinate oxysterols. Our model predicts that the putative 25-/27-HC-Tspan6 interface is stabilized by a series of non-polar interactions involving aromatic and non-aromatic residues. Some of these key residues (e.g., Val70 and Tyr93) are not conserved in other tetraspanins, which may explain why Tspan4 does not emulate Tspan6 activity in migration experiments. Furthermore, our preliminary experiments indicate that the C-terminal part of Tspan6, which controls intracellular trafficking of the protein, may also play a role in the regulation of its function toward cellular oxysterols.

While in this study we specifically focused on the link between the expression of Tspan6 and accumulation of oxysterols in CCD-EVs, we cannot exclude that cancer-related changes in the expression levels of this protein have a wider effect on the composition and functionality of EVs. Indeed, we have recently reported that in colorectal cancer cells, Tspan6 controls recruitment of the transmembrane form of TGFα to EVs via syntenin-1.[43] Our current results show that glycosylation patterns of certain EV-associated transmembrane proteins may be affected by the expression of Tspan6 in BCa cells. Future investigation will be necessary to examine the full extent of the Tspan6-dependent changes in CCD-EVs.

In summary, we have revealed a mechanism of Tspan6-dependent regulation of the tumor immune microenvironment and this may have profound implications for drug development in the treatment of BCa.

Limitations of the study

Although here we have focused on molecular pathways of communication between BCa cells and B lymphocytes, the Tspan6-oxysterol-LXR signaling axis is likely to have a broad effect on the formation of the tumor microenvironment in BCa, and, perhaps, in other types of cancer. Interestingly, we observed an increased accumulation of macrophages in Tspan6-expressing mammary carcinomas in mice. As our results show that EVs secreted by BCa tumor cells (and LXR-dependent signaling) do not affect the migration of monocytes (which are thought to be precursors of tumor-associated macrophages), one can conclude that the Tspan6-dependent pathway is likely to affect differentiation of monocytes to macrophages. Indeed, previous studies indicated that 27-HC and LXR activation have a variety of pleiotropic effects on the survival and functionality of macrophages and other types of immune cells that are typically found in the tumor microenvironment.[44,45] Detailed characterization of the LXR-induced signaling networks in different tumor-associated cell types will be necessary to fully assess the impact of Tspan6-oxysterol-LXR signaling on the formation and progression-dependent changes in the immune microenvironment in BCa. Our data strongly suggest that Tspan6 directly binds/coordinates 25- and 27-hydroxycholesterols and regulates their accumulation in EVs. Further investigation will be required to establish specific molecular aspects of Tspan6-oxysterol interactions and identify Tspan6-dependent pathways responsible for trafficking oxysterols to EVs.

STAR★METHODS

Detailed methods are provided in the online version of this paper and include the following:

- KEY RESOURCES TABLE
- RESOURCE AVAILABILITY
  - Lead contact
  - Materials availability
  - Data and code availability
- EXPERIMENTAL MODEL AND SUBJECT DETAILS
  - Ethics statement
  - Mice and tumor initiation
  - Kaede mice and E0771 tumors
  - Cell isolation for E0771/E0771^{Tspan6} Kaede experiments
  - Cell line models
  - Human subjects
- METHODS DETAILS
  - Immunohistochemistry (IHC), evaluation of staining and scoring systems
  - Isolation of PBMCs and PBMC transmigration experiments
  - Flow cytometry
  - Isolation of EVs
  - Analysis of EVs secreted by BCa cells
  - Western blotting
  - Analysis of cytokine and chemokine production
  - Mass spectrometry analysis of oxysterols
  - Structural modeling of Tspan6
  - Molecular docking of 25-HC and 27-HC with Tspan6
  - RNA sequencing (RNA-seq) and bioinformatics analysis
- QUANTIFICATION AND STATISTICAL ANALYSIS

SUPPLEMENTAL INFORMATION

Supplemental information can be found online at https://doi.org/10.1016/j.celrep.2023.112207.

ACKNOWLEDGMENTS

We are grateful to Dr. O. Yoshie, Dr. E. Rubinstein, and Dr. S. Charrin for providing anti-tetraspanin mAbs. This work was supported by MRC grant (to F.B., A.M.S., and H.M.L.), the Inflammatory Breast Cancer Network UK (to F.B.), and Ministry of Higher Education and Research, Egypt (N.B.). A.M.S. is supported by the Birmingham CRUK Centre. I.H.K.D. acknowledges funding from Aston Medical School. F.M. is supported by Wellcome Trust grant 099266/Z/12/Z.

AUTHOR CONTRIBUTIONS

Conceptualization – H.M.L. and F.B.; Methodology – G.M., H.M.L., D.R.W, S.v.L., F.M., I.N., A.M.S., I.H.K.D., and F.B.; Validation – G.M., H.M.L., V.N., S.H., N.B., M.G., I. Danial, I. Dean, F.M., I.N., L.P., S.v.L., A.M.S., I.H.K.D., and F.B.; Formal Analysis – G.M., H.M.L., M.G., I. Danial, N.B., I. Dean, F.M., I.N., L.P., S.v.L., A.M.S., I.H.K.D., and F.B.; Resources – F.B., A.H., V.S., A.M.S., I.H.K.D., and H.M.L.; Writing—Original Draft, G.M., H.M.L., I.H.D.K., S.v.L., and F.B.; Writing—Review and Editing, D.R.W., H.M.L., F.M., I.N., A.M.S., N.B., A.H., V.S., S.v.L., and F.B.; Supervision – D.R.W.,

H.M.L., I.N., A.M.S., and F.B.; Project Administration – H.M.L. and F.B.; Funding Acquisition – H.M.L., A.M.S., I.H.K.D., and F.B.

DECLARATION OF INTERESTS

The authors declare no competing interests.

Received: June 6, 2022
Revised: January 11, 2023
Accepted: February 15, 2023

REFERENCES

1. Mao, Y., Keller, E.T., Garfield, D.H., Shen, K., and Wang, J. (2013). Stromal cells in tumor microenvironment and breast cancer. Cancer Metastasis Rev. *32*, 303–315. https://doi.org/10.1007/s10555-012-9415-3.
2. Jiang, X., and Shapiro, D.J. (2014). The immune system and inflammation in breast cancer. Mol. Cell. Endocrinol. *382*, 673–682. https://doi.org/10.1016/j.mce.2013.06.003.
3. Badr, N.M., Berditchevski, F., and Shaaban, A.M. (2020). The immune microenvironment in breast carcinoma: predictive and prognostic role in the neoadjuvant setting. Pathobiology *87*, 61–74. https://doi.org/10.1159/000504055.
4. Nielsen, J.S., and Nelson, B.H. (2012). Tumor-infiltrating B cells and T cells: working together to promote patient survival. OncoImmunology *1*, 1623–1625. https://doi.org/10.4161/onci.21650.
5. Nielsen, J.S., Sahota, R.A., Milne, K., Kost, S.E., Nesslinger, N.J., Watson, P.H., and Nelson, B.H. (2012). CD20+ tumor-infiltrating lymphocytes have an atypical CD27- memory phenotype and together with CD8+ T cells promote favorable prognosis in ovarian cancer. Clin. Cancer Res. *18*, 3281–3292. https://doi.org/10.1158/1078-0432.CCR-12-0234.
6. Mahmoud, S.M.A., Lee, A.H.S., Paish, E.C., Macmillan, R.D., Ellis, I.O., and Green, A.R. (2012). The prognostic significance of B lymphocytes in invasive carcinoma of the breast. Breast Cancer Res. Treat. *132*, 545–553. https://doi.org/10.1007/s10549-011-1620-1.
7. Garaud, S., Buisseret, L., Solinas, C., Gu-Trantien, C., de Wind, A., Van den Eynden, G., Naveaux, C., Lodewyckx, J.N., Boisson, A., Duvillier, H., et al. (2019). Tumor infiltrating B-cells signal functional humoral immune responses in breast cancer. JCI Insight *5*, e129641. https://doi.org/10.1172/jci.insight.129641.
8. Qin, Y., Peng, F., Ai, L., Mu, S., Li, Y., Yang, C., and Hu, Y. (2021). Tumor-infiltrating B cells as a favorable prognostic biomarker in breast cancer: a systematic review and meta-analysis. Cancer Cell Int. *21*, 310. https://doi.org/10.1186/s12935-021-02004-9.
9. Hollern, D.P., Xu, N., Thennavan, A., Glodowski, C., Garcia-Recio, S., Mott, K.R., He, X., Garay, J.P., Carey-Ewend, K., Marron, D., et al. (2019). B cells and T follicular helper cells mediate response to checkpoint inhibitors in high mutation burden mouse models of breast cancer. Cell *179*, 1191–1206.e21. https://doi.org/10.1016/j.cell.2019.10.028.
10. Pimenta, E.M., and Barnes, B.J. (2014). Role of tertiary lymphoid structures (TLS) in anti-tumor immunity: potential tumor-induced cytokines/chemokines that regulate TLS formation in epithelial-derived cancers. Cancers *6*, 969–997. https://doi.org/10.3390/cancers6020969.
11. Tkach, M., and Théry, C. (2016). Communication by extracellular vesicles: where we are and where we need to go. Cell *164*, 1226–1232. https://doi.org/10.1016/j.cell.2016.01.043.
12. Bhatta, B., and Cooks, T. (2020). Reshaping the tumor microenvironment: extracellular vesicles as messengers of cancer cells. Carcinogenesis *41*, 1461–1470. https://doi.org/10.1093/carcin/bgaa107.
13. de Freitas, F.A., Levy, D., Reichert, C.O., Cunha-Neto, E., Kalil, J., and Bydlowski, S.P. (2022). Effects of oxysterols on immune cells and related diseases. Cells *11*. https://doi.org/10.3390/cells11081251.
14. Griffiths, W.J., and Wang, Y. (2022). Cholesterol metabolism: from lipidomics to immunology. J. Lipid Res. *63*, 100165. https://doi.org/10.1016/j.jlr.2021.100165.
15. Ma, L., Cho, W., and Nelson, E.R. (2022). Our evolving understanding of how 27-hydroxycholesterol influences cancer. Biochem. Pharmacol. *196*, 114621. https://doi.org/10.1016/j.bcp.2021.114621.
16. Andreu, Z., and Yáñez-Mó, M. (2014). Tetraspanins in extracellular vesicle formation and function. Front. Immunol. *5*, 442. https://doi.org/10.3389/fimmu.2014.00442.
17. Nazarenko, I., Rana, S., Baumann, A., McAlear, J., Hellwig, A., Trendelenburg, M., Lochnit, G., Preissner, K.T., and Zöller, M. (2010). Cell surface tetraspanin Tspan8 contributes to molecular pathways of exosome-induced endothelial cell activation. Cancer Res. *70*, 1668–1678. https://doi.org/10.1158/0008-5472.CAN-09-2470.
18. Park, S.M., Brooks, A.E., Chen, C.J.J., Sheppard, H.M., Loef, E.J., McIntosh, J.D., Angel, C.E., Mansell, C.J., Bartlett, A., Cebon, J., et al. (2021). Migratory cues controlling B-lymphocyte trafficking in human lymph nodes. Immunol. Cell Biol. *99*, 49–64. https://doi.org/10.1111/imcb.12386.
19. Lu, E., and Cyster, J.G. (2019). G-protein coupled receptors and ligands that organize humoral immune responses. Immunol. Rev. *289*, 158–172. https://doi.org/10.1111/imr.12743.
20. Kehrl, J.H. (2016). The impact of RGS and other G-protein regulatory proteins on Galphai-mediated signaling in immunity. Biochem. Pharmacol. *114*, 40–52. https://doi.org/10.1016/j.bcp.2016.04.005.
21. Hayward, S., Gachehiladze, M., Badr, N., Andrijes, R., Molostvov, G., Paniushkina, L., Sopikova, B., Slobodová, Z., Mgebrishvili, G., Sharma, N., et al. (2020). The CD151-midkine pathway regulates the immune microenvironment in inflammatory breast cancer. J. Pathol. *251*, 63–73. https://doi.org/10.1002/path.5415.
22. Sung, B.H., Parent, C.A., and Weaver, A.M. (2021). Extracellular vesicles: critical players during cell migration. Dev. Cell *56*, 1861–1874. https://doi.org/10.1016/j.devcel.2021.03.020.
23. Choi, C., and Finlay, D.K. (2020). Diverse immunoregulatory roles of oxysterols-the oxidized cholesterol metabolites. Metabolites *10*, 384. https://doi.org/10.3390/metabo10100384.
24. Beceiro, S., Pap, A., Czimmerer, Z., Sallam, T., Guillén, J.A., Gallardo, G., Hong, C., A-Gonzalez, N., Tabraue, C., Diaz, M., et al. (2018). Liver X receptor nuclear receptors are transcriptional regulators of dendritic cell chemotaxis. Mol. Cell Biol. *38*, e00534-17. https://doi.org/10.1128/MCB.00534-17.
25. Bensinger, S.J., Bradley, M.N., Joseph, S.B., Zelcer, N., Janssen, E.M., Hausner, M.A., Shih, R., Parks, J.S., Edwards, P.A., Jamieson, B.D., and Tontonoz, P. (2008). LXR signaling couples sterol metabolism to proliferation in the acquired immune response. Cell *134*, 97–111. https://doi.org/10.1016/j.cell.2008.04.052.
26. Heine, G., Dahten, A., Hilt, K., Ernst, D., Milovanovic, M., Hartmann, B., and Worm, M. (2009). Liver X receptors control IgE expression in B cells. J. Immunol. *182*, 5276–5282. https://doi.org/10.4049/jimmunol.0801804.
27. Record, M., Attia, M., Carayon, K., Pucheu, L., Bunay, J., Soulès, R., Ayadi, S., Payré, B., Perrin-Cocon, L., Bourgailh, F., et al. (2022). Targeting the liver X receptor with dendrogenin A differentiates tumour cells to secrete immunogenic exosome-enriched vesicles. J. Extracell. Vesicles *11*, e12211. https://doi.org/10.1002/jev2.12211.
28. Juhl, A.D., Lund, F.W., Jensen, M.L.V., Szomek, M., Heegaard, C.W., Guttmann, P., Werner, S., McNally, J., Schneider, G., Kapishnikov, S., and Wüstner, D. (2021). Niemann Pick C2 protein enables cholesterol transfer from endo-lysosomes to the plasma membrane for efflux by shedding of extracellular vesicles. Chem. Phys. Lipids *235*, 105047. https://doi.org/10.1016/j.chemphyslip.2020.105047.
29. Charrin, S., Manié, S., Thiele, C., Billard, M., Gerlier, D., Boucheix, C., and Rubinstein, E. (2003). A physical and functional link between cholesterol and tetraspanins. Eur. J. Immunol. *33*, 2479–2489.

30. Zimmerman, B., Kelly, B., McMillan, B.J., Seegar, T.C.M., Dror, R.O., Kruse, A.C., and Blacklow, S.C. (2016). Crystal structure of a full-length human tetraspanin reveals a cholesterol-binding pocket. Cell *167*, 1041–1051.e11. https://doi.org/10.1016/j.cell.2016.09.056.

31. Mackley, E.C., Houston, S., Marriott, C.L., Halford, E.E., Lucas, B., Cerovic, V., Filbey, K.J., Maizels, R.M., Hepworth, M.R., Sonnenberg, G.F., et al. (2015). CCR7-dependent trafficking of RORgamma(+) ILCs creates a unique microenvironment within mucosal draining lymph nodes. Nat. Commun. *6*, 5862. https://doi.org/10.1038/ncomms6862.

32. Opzoomer, J.W., Anstee, J.E., Dean, I., Hill, E.J., Bouybayoune, I., Caron, J., Muliaditan, T., Gordon, P., Sosnowska, D., Nuamah, R., et al. (2021). Macrophages orchestrate the expansion of a proangiogenic perivascular niche during cancer progression. Sci. Adv. *7*, eabg9518. https://doi.org/10.1126/sciadv.abg9518.

33. Fakheri, R.J., and Javitt, N.B. (2012). 27-Hydroxycholesterol, does it exist? On the nomenclature and stereochemistry of 26-hydroxylated sterols. Steroids *77*, 575–577. https://doi.org/10.1016/j.steroids.2012.02.006.

34. Roberg-Larsen, H., Lund, K., Seterdal, K.E., Solheim, S., Vehus, T., Solberg, N., Krauss, S., Lundanes, E., and Wilson, S.R. (2017). Mass spectrometric detection of 27-hydroxycholesterol in breast cancer exosomes. J. Steroid Biochem. Mol. Biol. *169*, 22–28. https://doi.org/10.1016/j.jsbmb.2016.02.006.

35. Bawono, P., and Heringa, J. (2014). PRALINE: a versatile multiple sequence alignment toolkitP. Methods Mol Biol *1079*, 245–262.

36. Xie, F., Zhou, X., Fang, M., Li, H., Su, P., Tu, Y., Zhang, L., and Zhou, F. (2019). Extracellular vesicles in cancer immune microenvironment and cancer immunotherapy. Adv. Sci. *6*, 1901779. https://doi.org/10.1002/advs.201901779.

37. Shen, M., Wang, J., and Ren, X. (2018). New insights into tumor-infiltrating B lymphocytes in breast cancer: clinical impacts and regulatory mechanisms. Front. Immunol. *9*, 470. https://doi.org/10.3389/fimmu.2018.00470.

38. Salmi, M., and Jalkanen, S. (2014). Ectoenzymes in leukocyte migration and their therapeutic potential. Semin. Immunopathol. *36*, 163–176. https://doi.org/10.1007/s00281-014-0417-9.

39. Huang, Y., Fu, X., Lyu, X., Xu, Z., He, Z., Zhang, Y., Zeng, Y., He, F., and Huang, G. (2015). Activation of LXR attenuates collagen-induced arthritis via suppressing BLyS production. Clin. Immunol. *161*, 339–347. https://doi.org/10.1016/j.clim.2015.09.015.

40. Ramón-Vázquez, A., de la Rosa, J.V., Tabraue, C., Lopez, F., Díaz-Chico, B.N., Bosca, L., Tontonoz, P., Alemany, S., and Castrillo, A. (2019). Common and differential transcriptional actions of nuclear receptors liver X receptors alpha and beta in macrophages. Mol. Cell Biol. *39*, e00376-18. https://doi.org/10.1128/MCB.00376-18.

41. Kalra, H., Simpson, R.J., Ji, H., Aikawa, E., Altevogt, P., Askenase, P., Bond, V.C., Borràs, F.E., Breakefield, X., Budnik, V., et al. (2012). Vesiclepedia: a compendium for extracellular vesicles with continuous community annotation. PLoS Biol. *10*, e1001450. https://doi.org/10.1371/journal.pbio.1001450.

42. Hurwitz, S.N., Rider, M.A., Bundy, J.L., Liu, X., Singh, R.K., and Meckes, D.G., Jr. (2016). Proteomic profiling of NCI-60 extracellular vesicles uncovers common protein cargo and cancer type-specific biomarkers. Oncotarget *7*, 86999–87015. https://doi.org/10.18632/oncotarget.13569.

43. Andrijes, R., Hejmadi, R.K., Pugh, M., Rajesh, S., Novitskaya, V., Ibrahim, M., Overduin, M., Tselepis, C., Middleton, G.W., Győrffy, B., et al. (2021). Tetraspanin 6 is a regulator of carcinogenesis in colorectal cancer. Proc. Natl. Acad. Sci. USA *118*, e2011411118. https://doi.org/10.1073/pnas.2011411118.

44. Shahoei, S.H., and Nelson, E.R. (2019). Nuclear receptors, cholesterol homeostasis and the immune system. J. Steroid Biochem. Mol. Biol. *191*, 105364. https://doi.org/10.1016/j.jsbmb.2019.04.013.

45. Schulman, I.G. (2017). Liver X receptors link lipid metabolism and inflammation. FEBS Lett. *591*, 2978–2991. https://doi.org/10.1002/1873-3468.12702.

46. Berditchevski, F., Chang, S., Bodorova, J., and Hemler, M.E. (1997). Generation of monoclonal antibodies to integrin-associated proteins. Evidence that alpha3beta1 complexes with EMMPRIN/basigin/OX47/M6. J. Biol. Chem. *272*, 29174–29180.

47. Tachibana, I., Bodorova, J., Berditchevski, F., Zutter, M.M., and Hemler, M.E. (1997). NAG-2, a novel transmembrane-4 superfamily (TM4SF) protein that complexes with integrins and other TM4SF proteins. J. Biol. Chem. *272*, 29181–29189.

48. Imai, T., Fukudome, K., Takagi, S., Nagira, M., Furuse, M., Fukuhara, N., Nishimura, M., Hinuma, Y., and Yoshie, O. (1992). C33 antigen recognized by monoclonalantibodies inhibitory to human T cell leukemia virus type 1-induced syncytium formation is a member of a new family of transmembrane proteins including CD9, CD37, CD53, and CD63. J. Immunol. *149*, 2879–2886.

49. Imai, T., and Yoshie, O. (1993). C33 antigen and M38 antigen recognized by monoclonal antibodies inhibitory to syncytium formation by human T cell leukemia virus type 1 are both members of the transmembrane 4 superfamily and associate with each other and with CD4 and CD8 in T cells. J. Immunol. *151*, 6470–6481.

50. Garcia, R., Yu, C.L., Hudnall, A., Catlett, R., Nelson, K.L., Smithgall, T., Fujita, D.J., Ethier, S.P., and Jove, R. (1997). Constitutive activation of Stat3 in fibroblasts transformed by diverse oncoproteins and in breast carcinoma cells. Cell Growth Differ. *8*, 1267–1276.

51. Waldmeier, L., Meyer-Schaller, N., Diepenbruck, M., and Christofori, G. (2012). Py2T murine breast cancer cells, a versatile model of TGFbeta-induced EMT in vitro and in vivo. PLoS One *7*, e48651. https://doi.org/10.1371/journal.pone.0048651.

52. Garaud, S., Gu-Trantien, C., Lodewyckx, J.N., Boisson, A., De Silva, P., Buisseret, L., Migliori, E., Libin, M., Naveaux, C., Duvillier, H., and Willard-Gallo, K. (2014). A simple and rapid protocol to non-enzymatically dissociate fresh human tissues for the analysis of infiltrating lymphocytes. JoVE *10*, 52392.

53. Tomura, M., Yoshida, N., Tanaka, J., Karasawa, S., Miwa, Y., Miyawaki, A., and Kanagawa, O. (2008). Monitoring cellular movement in vivo with photoconvertible fluorescence protein "Kaede" transgenic mice. Proc. Natl. Acad. Sci. USA *105*, 10871–10876. https://doi.org/10.1073/pnas.0802278105.

54. Dutton, E.E., Gajdasik, D.W., Willis, C., Fiancette, R., Bishop, E.L., Camelo, A., Sleeman, M.A., Coccia, M., Didierlaurent, A.M., Tomura, M., et al. (2019). Peripheral lymph nodes contain migratory and resident innate lymphoid cell populations. Sci. Immunol. *4*, eaau8082. https://doi.org/10.1126/sciimmunol.aau8082.

55. Pinder, S.E., Brown, J.P., Gillett, C., Purdie, C.A., Speirs, V., Thompson, A.M., and Shaaban, A.M.; Translational Subgroup of the NCRI Breast Clinical Studies Group (2013). The manufacture and assessment of tissue microarrays: suggestions and criteria for analysis, with breast cancer as an example. J. Clin. Pathol. *66*, 169–177. https://doi.org/10.1136/jclinpath-2012-201091.

56. Dias, I.H.K., Milic, I., Lip, G.Y.H., Devitt, A., Polidori, M.C., and Griffiths, H.R. (2018). Simvastatin reduces circulating oxysterol levels in men with hypercholesterolaemia. Redox Biol. *16*, 139–145. https://doi.org/10.1016/j.redox.2018.02.014.

57. Zhang, Y. (2008). I-TASSER server for protein 3D structure prediction. BMC Bioinf. *9*, 40. https://doi.org/10.1186/1471-2105-9-40.

58. van Zundert, G.C.P., Rodrigues, J.P.G.L.M., Trellet, M., Schmitz, C., Kastritis, P.L., Karaca, E., Melquiond, A.S.J., van Dijk, M., de Vries, S.J., and Bonvin, A.M.J.J. (2016). The HADDOCK2.2 web server: user-friendly integrative modeling of biomolecular complexes. J. Mol. Biol. *428*, 720–725. https://doi.org/10.1016/j.jmb.2015.09.014.

STAR★METHODS

KEY RESOURCES TABLE

REAGENT or RESOURCE	SOURCE	IDENTIFIER
Antibodies		
Mouse anti-human CD14, clone HCD14	BioLegend	325607
Mouse anti-human CD19, clone HIB19	BioLegend	302216
Mouse anti-human CD24, clone SN3 A5-H10	ThermoFisher	17-0247-42
Mouse anti-human CD27, clone M-T271	BD Bioscience	555441
Mouse anti-human CD27, clone M-T271	BioLegend	356410
Mouse anti-human CD3, clone SK7	BD Bioscience	339186
Mouse anti-human CD38, clone HIT2	BioLegend	303510
Mouse anti-human CD4, clone SFCI12T4D11	Beckman coulter	6604727
Mouse anti-human CD8, clone RPA-T8	BD Bioscience	555367
Mouse anti-human IgD, clone IA6-2	BioLegend	348206
Rat anti-mouse B220, clone RA3-6B2	BD Bioscience	563793
Armenian hamster anti-mouse CD11c, clone N418	BioLegend	117347
Rat anti-mouse CD11b, clone M1/70	ThermoFisher	25-0112-82
Rat anti-mouse CD3, clone 17A2	ThermoFisher	11-0032-82
Rat anti-mouse CD3, clone 17A2	Biolegend	100236
Rat anti-mouse CD38, clone 90	BioLegend	102727
Armenian hamster anti-mouse CD3e, clone 145-2C11	BD Bioscience	612771
Rat anti-mouse CD4, clone RM4-5	BioLegend	100551
Rat anti-mouse CD4, clone GK1.5	Southern Biotech	1540–10
Rat anti-mouse CD45, clone 30-F11	BioLegend	103139
Rat anti-mouse CD8, clone 53–6.7	BioLegend	100721
Rat anti-mouse F4/80, clone BM8	ThermoFisher	50-4801-82
Rat anti-mouse F4/80, clone BM8	ThermoFisher	12-4801-82
Rat anti-mouse FoxP3, clone FJK16s	ThermoFisher	48-5773-80
Rat anti-mouse LY-6C, clone HK1.4	BioLegend	128037
Rat anti-mouse LY-6G, clone 1A8	BioLegend	108441
Rat anti-mouse MHC class II, clone m5/114.15.2	BioLegend	107635
Mouse anti-human/mouse Tspan6, polyclonal	Customly produced	N/A
Rabbit anti-human Tspan6, polyclonal	Sigma Aldrich	HPA004109
Mouse anti-human CD20, clone L26	ThermoFisher	MA5-13141
Rabbit anti-human Tspan6, polyclonal	Abcepta	AP9224b
Mouse anti-human CD63, clone E−12	Santa Cruz	sc-365604
Rabbit ant-GFP, polyclonal	ThermoFisher	A6455
Mouse anti-human Tspan24/CD151, clone 5C11	Reported in[46]	N/A
Mouse anti-human Tspan4, clone NAG-2	Reported in[47]	N/A
Mouse anti-human Tspan27/CD82, clone M104	Dr.O.Yoshie[48]	N/A
Mouse anti-human Tspan28/CD81, clone M38	Dr.O.Yoshie[49]	N/A
Mouse anti-human Tspan13, clone TS13-1	Dr.E.Rubinstein; this paper	N/A
Deposited data		
RNA seq	This paper	BioStudies Submission - E-MTAB-12362
Biological samples		
Blood from healthy and breast cancer patients	University of Birmimngham	N/A

(*Continued on next page*)

Continued

REAGENT or RESOURCE	SOURCE	IDENTIFIER
Experimental models: Cell lines		
SUM149	Garcia et al.[50]	N/A
MDA-MB-468	ATCC	HTB-132
MCF-7	ATCC	HTB-22
SKBr3	ATCC	HTB-30
HCC70	ATCC	CRL-2315
E0771	CH3 BioSystems	SKU: 94A001
Py2T	Waldmeier et al.[51]	N/A
MDA-MB-468/pLVx	This paper	N/A
MDA-MB-468/Tspan6	This paper	N/A
MDA-MB-468/Tspan6-Oxy	This paper	N/A
MDA-MB-468/GFP	This paper	N/A
MDA-MB-468/GFP-Tspan6	This paper	N/A
MDA-MB-468/GFP-Tspan6-Oxy	This paper	N/A
SKBr3/pLVx	This paper	N/A
SKBr3/Tspan6	This paper	N/A
Py2T/pLVx	This paper	N/A
Py2T/Tspan6	This paper	N/A
E0771/pLVx	This paper	N/A
E0771/Tspan6	This paper	N/A
MCF7/GFP	This paper	N/A
MCF7/GFP-Tspan6	This paper	N/A
MCF7/GFP-Tspan6-Oxy	This paper	N/A
SUM149PT/GFP	This paper	N/A
SUM149PT/GFP-Tspan4	This paper	N/A
SUM149PT/GFP-Tspan6	This paper	N/A
SUM149PT/GFP-Tspan13	This paper	N/A
SUM149PT/GFP-Tspan27	This paper	N/A
SUM149PT/GFP-Tspan24	This paper	N/A
HCC70/pLKO	This paper	N/A
HCC70/shT6-1	This paper	N/A
HCC70/shT6-2	This paper	N/A
Experimental models: organisms/strains		
Mouse: C.Cg-Tg(CAG-tdKaede)15Utr (BALB/c background)	RIKEN BioResource Center	RBRC09257
Mouse: FVB/NJ	The Jackson Laboratories	RRID:IMSR_JAX:001,800

RESOURCE AVAILABILITY

Lead contact

Further information and requests for resources and reagents should be directed to and will be fulfilled by the lead contact, Fedor Berditchevski (f.berditchevski@bham.ac.uk).

Materials availability

There are no restrictions to the availability of tools generated in this study.

Data and code availability

- RNA-seq data have been deposited at BioStudies and are publicly available as of the date of publication. The accession number is listed in the key resources table.
- This paper does not report the original code

- Any additional information required to reanalyse the data reported in this paper is available from the lead contact upon request.

EXPERIMENTAL MODEL AND SUBJECT DETAILS

Ethics statement

Mice were used in accordance with Home Office guidelines at the University of Birmingham under a Project Licence awarded to D.R.W. and approved by the University of Birmingham Animal Welfare and Ethical Review Body. Mice were housed at 21 ± 2°C, 55% humidity (±10%), with 12 h light-dark/cycle in 7–7 individually ventilated caging with environmental enrichment of plastic houses plus paper bedding.

Mice and tumor initiation

Murine PY2T-pLVx/Tspan6 tumors

6 week old FVB female mice were bilaterally injected into the mammary fat pads with PY2T-pLVx or PY2T-Tspan6 (1×10^6 cells/100μL PBS per injection). Once the developing tumors had reached 200 mm^3 in volume (typically 4 weeks), the animals were humanely killed. Removed tumors were weighed and non-enzymatically homogenised using a Gentle Macs Dissociator (Miltenyi Biotec) to extract TIL.[52] Isolated TIL were washed, stained and analyzed by multi-colour flow cytometry (below). The absolute number of TIL per mg of tumor was determined using CountBright Absolute Counting Beads (Invitrogen).

Kaede mice and E0771 tumors

C57BL/6 Kaede[53] mice were maintained and bred at the University of Birmingham Biomedical Services Unit. Mice were culled between the ages of 7 and 15 weeks. E0771 cells grown in log phase were then harvested and suspended in Dulbecco's Phosphate Buffered Saline (DPBS, Sigma, D8662), and 100 μL of cell suspension containing 2.5×10^5 cells were subcutaneously injected into the mammary fat pad of female mice under anesthesia via 2% gaseous isoflurane.

E0771/E0771^{Tspan6} tumors were grown in C57BL/6 Kaede mice for 11 days until tumor size reached approximately 60–80mm.[3] Photoconversion of the 'Kaede Green' protein to the converted 'Kaede Red' version was achieved by exposing tumors to a 405nm LED light using a Dymax BlueWave QX4 system (DYM41572, Intertronics) set to 50% power through an 8mm focusing lens for a total of 3 min consisting of 9–20 s exposure cycles with 5-s breaks between each exposure cycle (adapted from[54]). Tumors were excised for flow cytometric analysis 48 h after photoconversion.

Cell isolation for E0771/E0771^{Tspan6} Kaede experiments

Tumor were cut into 1-2mm pieces and incubated with 1 mg/mL Collagenase D (11,088,882,001, Roche) and 0.1 mg/mL DNase I (101,104,159,001, Roche), in 1mL RPMI media for 20 min at 37°C on a thermomixer (Eppendorf). After enzymatic digestion samples were crushed through a 100μm cell strainer before removing large debris by further filtering samples through a 70μm cell strainer. Spleens were crushed through a 70μm cell strainer then incubated in 5mL Gey's red blood cell lysis buffer on ice for 5 min. Tumor draining, and contralateral lymph nodes (axillary and brachial combined) were cut into fine pieces then passed through a 70μm cell strainer. Isolated cells were centrifuged at 400 g at 4°C for 5 min and resuspended in 200μL FACS staining buffer (2% FBS, 2mM EDTA in PBS).

Cell line models

Human breast cancer cell lines MDA-MB-468, MCF7, HCC70 and SKBr3 and 293T cells were obtained from the ATCC. Mouse mammary carcinoma cell line EO771 was purchased from the CH3 BioSystems (Amherst, NY). Human breast cancer cell line SUM149PT was a kind gift from Dr. Stephen P. Ethier (now available from Asterand, Detroit, MI). Mouse mammary carcinoma cell line Py2T[51] was provided by Dr.G.Christofori (University of Basel). All cell lines except for MCF7, HCC70, and SUM149PT were maintained in complete DMEM (Gibco or Sigma) supplemented with 10% fetal calf serum (FCS), 100 I.U./mL penicillin and 100 μg/mL streptomycin. MCF7 and HCC70 cells were grown in RPMI-1640 (Gibco or Sigma) supplemented with 10% fetal calf serum (FCS), 100 I.U./mL penicillin and 100 μg/mL streptomycin. SUM149PT cells were maintained in Ham's F12 Nutrient Mix containing 10%FCS, 5U/mL penicillin/streptomycin (Gibco), 5 μg/mL insulin (Sigma), and 1 μg/mL hydrocortisone (Sigma). All cell lines were confirmed to be negative for mycoplasma (MycoAlert Detection Kit, Lonza LT07-418).

To establish the SUM149-GFP-tetraspanin cell panel, SUM149PT cells were infected with pLVx-IRES-puro–based lentiviruses encoding GFP-tagged tetraspanin proteins; SUM149PT cells were infected with the pLVx-IRES-puro-GFP lentivirus to establish the SUM149/GFP cell line. GFP-positive SUM149PT cells were subsequently selected after cell sorting. MDA-MB-468/GFP, MDA-MB-468/GFP-Tspan6, MDA-MB-468/GFP-Tspan6-Oxy, MCF7/GFP, MCF7/GFP-Tspan6 and MCF7/GFP-Tspan6-Oxy cell lines were established by infecting parental cell lines with pLVx-IRES-puro-GFP, pLVx-IRES-puro-GFP-Tspan6 and pLVx-IRES-puro-GFP-Tspan6-Oxy lentiviruses produced by 293T cells and subsequent selection in puromycin-containing growth media. E0771/Tspan6, MDA-MB-468/Tspan6, MDA-MB-468/Tspan6-Oxy, SUM149/Tspan6, SKBr3/TspanT6 and PY2T/Tspan6 cell lines were established by infecting parental cells (i.e. MDA-MB-468, SUM149PT, SKBr3, E0771 and PY2T) with pLVx-IRES-puro–based lentiviruses encoding either human (MDA-MB-468 and SKBr3) or mouse (E0771 and PY2T) Tspan6 or Tspan6-Oxy(-) mutant. Control cell

lines MDA468/pLVx, SKBr3/pLVx, E0771/pLVx and PY2T/pLVx were established by infecting parental cells with the pLVx-IRES-puro lentivirus. HCC70/shT6-1 and HCC70/shT6-2 cells were generated by infecting HCC70 cells with the pLKO-1 – based lentiviruses encoding shRNAs targeting human Tspan6 gene (Sigma Aldrich). The control HCC70/pLKO line was established by infecting the parental cell line with the pLKO.1 virus. After lentiviral gene transduction cells were selected on puromycin-containing growth media and subsequently used as pooled puromycin-resistant clones. For cell migration experiments, cells were plated at 8×10^5 (MDA-MB-468), 6×10^5 (SKBr3, MCF7, SUM149PT) or 4×10^5 (PY2T) cells per $25cm^2$ flask in 5 mL of growth media and cultured for 72 h. After culture the conditioned medium was collected, spun at 1500 rpm for 10 min to remove cell debris, filtered via 0.2μ and used for trans-migration assays.

Human subjects

Ethical approval for this study was granted from Leeds (East) REC (06/Q1206/180) and West Midlands – Black Country NRES Committee (07/Q2702/24). Tissue microarrays (TMAs) were assembled, as previously described,[55] from 358 cases of female breast cancer diagnosed at the Leeds Teaching Hospitals NHS Trust between 1987 and 2005 with a mean follow-up of 80.5 months. After the exclusion of non-representative cores and core loss, a cohort of 263 BCa patients (24–76 years) was studied with the following tumor grades: 26 patients with grade 1, 126 – grade 2 and 111 – grade 3.

METHODS DETAILS

Immunohistochemistry (IHC), evaluation of staining and scoring systems

Formalin-fixed and paraffin-embedded (FFPE) tissue TMA blocks were sectioned for staining using a standard protocol. Sections were manually incubated with 100μL of primary antibody against Tspan6 for 1 h followed by incubation with a secondary antibody (ImmPRESS TM universal anti-mouse/rabbit Ig) for half an hour. Tumor infiltrating B-cells were identified using a ready to use mouse anti-CD20 mAb using the standard protocol for diagnostic testing in a UKAS accredited laboratory on the Dako Link 48 Autostainer.

IHC stained slides were evaluated and scored by two independent pathologists (A.M.S. and M.G.) including a specialist breast pathologist. Membranous Tspan6 immunoreactivity was scored semi-quantitatively as negative (0), weak (1+), moderate (2+) and strong (3+) (Figure S1) as follows. Tumors without any detectable Tspan6 positivity or with faint membranous positivity in $\leq$10% of tumor cells were considered as weak expression negative (0). Incomplete membranous staining, which was barely noticeable but present in >10% tumor cells was considered as weak expression (1+). Circumferential membranous staining that was incomplete and/or moderate and in >10% tumor cells or complete strong membranous staining in $\leq$10% tumor cells was considered as moderate expression (2+). Circumferential membranous staining that was complete, strong and in >10% of cells was considered as strong expression (3+). Finally, for statistical dichotomization, cases with negative or weak expression (scores 0,1+) were considered as negative and those with moderate or strong expression (scores 2+ and 3+) were considered as positive.

Isolation of PBMCs and PBMC transmigration experiments

Blood samples were diluted 1:1 in plain RPMI-1640 medium, carefully overlaid on 15mL Lymphoprep (Axis-Shield) in 50mL tubes and centrifuged at 1600rpm (without brake) for 25 min at room temperature. The upper layer containing serum and platelets was removed with a transfer pipette and the interface containing mononuclear cells was collected. The cells were then washed twice in RPMI-1640 and used for transmigration assays.

Isolated PBMCs were counted using a haemocytometer and resuspended in RPMI-1640 medium at concentration 1×10^7 cells/mL. 200μL of PBMC suspension was added on top of the 5μM pore membrane in a 24 well transwell insert (Corning) and incubated for 10 min at 37°C and 5% CO2 to allow the cells to settle down. 800μL of the conditioned medium was added to the bottom of the well of a 24 well plate and the insert carefully placed on top of it. After 16h incubation, the migrated cells were collected from the bottom of the well, counted and processed for flow cytometry analysis.

Flow cytometry

Multi-colour flow cytometry was performed using an LSRII flow cytometer with FACSDiva software (BD Biosciences) with at least 5,000 cells recorded in each sample. During acquisition lymphocytes and monocytes were gated using forward (FSC) and side scatter (SSC), with doublets and dead cells excluded as appropriate. For immunophenotyping, migrated PBMCs were collected, counted and stained with up to 8-colour combinations of the antibodies (key resource table). The cells were washed in MACS buffer and re-suspended in 50μL of MACS buffer containing a mixture of fluorophore-conjugated antibodies. After a 30′ incubation on ice in the dark for 30 min the cells were washed and re-suspended in 400 μL of MACS buffer for analysis. The samples were stored at 4°C in the dark and analyzed within 2h of staining. Gating strategy has been recently described in.[21] Multi-colour flow cytometry performed using Kaede samples were acquired using an LSR Fortessa X-20 (BD Biosciences) with FACSDiva software (BD Biosciences) with at least 200,000 cells recorded per sample. Kaede samples were incubated with anti-CD16/32 (2.4G2, BioLegend) to block Fc receptor binding, before staining for viable cells using Live/Dead Fixable Dead Cell Stain Kits (1:1000, L34960, ThermoFisher) for 15 min at 4°C. Antibodies against surface markers were diluted in FACS staining buffer and incubated on ice for 30 min. To calculate absolute cell numbers per sample, 1×10^4 blank counting particles (ACBP-100-00, Spherotech) were added to stained samples before data acquisition. Data was analyzed using FlowJo software. To analyze expression of tetraspanin proteins cells were

detached using TrypLE and subsequently incubated with unlabeled mouse mAbs (key resource table) for 1h at 4°C. Subsequently, cells were washed in PBS and incubated for 30′ at 4°C with Goat anti-Mouse IgG (H + L) conjugated to Alexa 488 in the dark. After subsequent washes, stained cells were analyzed immediately on an LSRII flow cytometer (Beckman Coulter) and using FlowJo software.

Isolation of EVs

EVs were purified from the culture supernatant of cells growing in complete medium supplemented with exosome-depleted FCS for 72 h. Conditioned medium was sequentially centrifuged at 600×g for 10 min, followed by 10,000×g rpm for 45 min using a type SS-34 rotor in a Sorvall Evolution RC centrifuge (Beckman Coulter, USA), and finally at 70,000×g for 2 h using a type 70Ti rotor in a Beckman Coulter Optima L-100 XP ultracentrifuge (Beckman Coulter, USA). The resulting EVs pellet was washed once with PBS and finally resuspended in 250 μL PBS.

Analysis of EVs secreted by BCa cells

The size distribution and concentration of EVs were measured by nanoparticle tracking analysis (NTA) using PMX110 (Particle Metrix, Starnberg, Germany). Media conditioned by MDA468/pLVx or MDA468/Tspan6 cells were diluted in 0.1 x PBS (pre-filtered using a 0.22μm filter) to a final volume of 1 mL. For each measurement, 11 positions were scanned, and 30 frames were captured per position with a medium speed. The following capturing settings were applied: camera sensitivity for all samples 85.0%, shutter speed range 70, scattering intensity 4.0, and cell temperature 25°C. The videos were analyzed using ZetaView Software (8.04.02, Starnberg, Germany) with the following parameters: maximum particle size 1000nm minimum particle size 10nm, and minimum particle brightness 20 AU (arbitrary units). Statistical analysis was performed using GraphPad Prism 8.1.0 (GraphPad Software,San Diego, US) and significance was calculated using Multiple *t* test with Holm-Sidak method.

Western blotting

Cells grown to 80–90% confluence were lysed in Laemmli buffer supplemented with 2 mM PMSF, 10 μg/mL aprotinin, 10 μg/mL leupeptin, 5 mM EGTA, 1 mM EDTA, 2 mM $Na_4P_2O_7$, 5 mM NaF and 5 mM Na_3VO_4. Samples containing equal amounts of protein per lane were loaded and resolved on 10% SDS-PAGE and then transferred onto a nitrocellulose membrane. The membranes were probed with specific antibodies (key resource table) as previously described. The infrared-tagged secondary antibodies were used to visualise the signals, and the images were captured and quantified using an LI-COR Odyssey scanning system.

Analysis of cytokine and chemokine production

Human Chemokine Array Kit (Catalog # ARY017) was purchased from R&D Systems. ELISA kits were purchased from Peprotech and assayed using manufacturer's protocols.

Mass spectrometry analysis of oxysterols

EV pellets were mixed with methanol (430 μL) and LC-MS grade water (70μL) and spiked with deuterated internal standards (1 ng 24HCd7, 1 ng 25HCd6 and 1 ng 27-HCd6). The mixture was vortexed and incubated in ice with sonication for 10′ in the presence of 4 mg/mL BHT before centrifugation at 14,000 × g for 10 min. Supernatants were transferred to new Eppendorf tubes and dried under vacuum, re-suspended in 40 μL of 50% aqueous methanol containing 0.1% formic acid and analyzed by Liquid chromatography-tandem mass spectrometry (LC-MS/MS) as previously described.[56] Acquired data were processed using Analyst Software (version 1.7.1, AB Sciex).

Structural modeling of Tspan6

The structure of Tspan6 (residues M1-V245) was generated using the I-TASSER (Iterative Threading ASSEmbly Refinement) server.[57] Briefly, the target sequence was initially threaded through the Protein DataBank (PDB) library by the LOMETS2 meta threading server system for template-based protein structure prediction. Continuous fragments were excised from LOMETS2 alignments and structurally reassembled by replica-exchange Monte Carlo algorithms. The simulation trajectories were then clustered and used as the preliminary state for second round I-TASSER assembly simulations. Finally, the lowest energy structural models were selected and optimised by fragment-guided molecular dynamic simulations to refine hydrogen-bonding interactions and eliminate steric clashes. Models were ranked based on their I-TASSER confidence (C) score (range −5 to +2 with a higher score correlating with an improved model).

Molecular docking of 25-HC and 27-HC with Tspan6

The interaction between Tspan6 and 25-/27-HC was modeled with HADDOCK.[58] Tspan6 residues were classified as active in 25-/27-HC binding based upon CD81 residues previously implicated in cholesterol binding. 'Passively involved' residues were selected automatically. The entire 25-/27-HC moiety was selected for use as ambiguous interaction restraints to drive the docking process.

RNA sequencing (RNA-seq) and bioinformatics analysis

RNA was extracted non-migrated B cells and from B cells migrated toward purified EVs secreted by MDA-MB-468 cells using the Arcturus picopure RNA isolation kit (Thermofisher Scientific #12204–1). cDNAs (generated from 5 ng of the total RNA) and libraries were prepared using Lexogen's QuantSeq 3′ mRNA-Seq Kit. Samples were sequenced on NextSeq 500/550 High Output Kit v2 (150 cycles) (FC-404-2002) at the Genomics Birmingham sequencing facility.

To evaluate molecular differences between migratory (MB) and non-migratory B cells (NMB), raw RNA-sequencing reads were mapped onto the human reference genome (hg38) using the splice-aware aligner HISAT2 and resulting SAM-files were converted into BAM-files using *samtools*. Reads overlapping with the positions of genes in the genome were counted using the *summariseOverlaps* function in the ''IntersectionNotEmpty'' mode (BioC-package *GenomicAlignments*). Raw reads were scaled for differences in library sizes using the TMM method (BioC-package *edgeR*) and differences in gene expression between migratory (MB) and non-migratory (NMB) cells were calculated using generalized linear models accounting for repeated measures after *voom*-transformation (BioC-package *limma*). Resulting vectors of p values were subjected to Virtual Inference of Protein-activity by Enriched Regulon analysis (BioC-package *viper*) using a regulon specific for B-cells (BioC-package *bcellViper*) and significant results were adjusted for pleiotropic effects using the *shadow*-function.

To evaluate the molecular profiles of breast cancer (BRCA) samples for mechanisms regulating B cell migration and infiltration, z-transformed gene expression profiles for 1,904 BRCA samples that are part of the METABRIC series were downloaded from the cBioPortal for cancer genomics (https://www.cbioportal.org). To obtain estimates of infiltrating B cells, expression data were deconvoluted using the ConsensusTME R-package in combination with the single sample gene set enrichment analysis (ssGSEA) algorithm. To calculate NR1H3 activity in B-cells and TSPAN6 activity in BRCA cells, ARACNe inferred regulons for human B-cells and BRCA cells were obtained from the BioC-packages bcellViper and aracne.networks respectively. Based on these regulons, the protein activity of NR1H3 and TSPAN6 in their respective cell types was virtually inferred using the BioC-package viper. Expression data of genes overexpressed in MB-cells were visualized in heatmap format using the R-package *pheatmap*.

QUANTIFICATION AND STATISTICAL ANALYSIS

For experiments involving human subjects Mann-Whitney and Kruskal-Wallis tests were used to compare phenotype densities between breast cancer patients in terms of clinical and pathological data. Two-tailed p values < 0.05 were considered statistically significant. The Kaplan-Meier method and multivariate Cox regression were used for survival analysis. OS was calculated as the duration in months between the date of diagnosis and the date of last follow-up or death. Experiments using Kaeda mice were performed twice, all other experiments involving mice were performed at least four times and the results were expressed as the mean ± SD or SEM. Statistical analysis was performed using descriptive statistics, two-tailed paired t test and one-way ANOVA followed by Tukey's multiple comparison tests. p values < 0.05 were considered as statistically significant. Kaplan-Meier analysis was performed using the ggsurvival package in R and the log Rank test was used to calculate p values.